Excitation-Wavelength-Dependent Photophysics of d⁸d⁸ Di-isocyanide Complexes

Martin Pižl,^{a,b} Bryan M. Hunter,^c Igor V. Sazanovich,^d Michael Towrie,^d Harry B. Gray,^{e,*} Stanislav Záliš,^{a,*} Antonín Vlček^{a,f,*}

- ^a J. Heyrovský Institute of Physical Chemistry, Academy of Sciences of the Czech Republic, CZ-18223 Prague, Czech Republic
- ^b Department of Inorganic Chemistry, University of Chemistry and Technology, Prague, Technická 5, CZ-166 28 Prague, Czech Republic
- ^c Rowland Institute at Harvard, Cambridge, Massachusetts, 02142, United States
- ^d Central Laser Facility, Research Complex at Harwell, STFC, Rutherford Appleton Laboratory, Harwell Oxford, Didcot, Oxfordshire, OX11 0QX, United Kingdom;
- ^e Beckman Institute, California Institute of Technology, Pasadena, California 91125, United States
- f Department of Chemistry, Queen Mary University of London, E1 4NS London, United Kingdom;

Corresponding authors' e-mails: hbgray@caltech.edu, zalis@jh-inst.cas.cz, a.vlcek@qmul.ac.uk

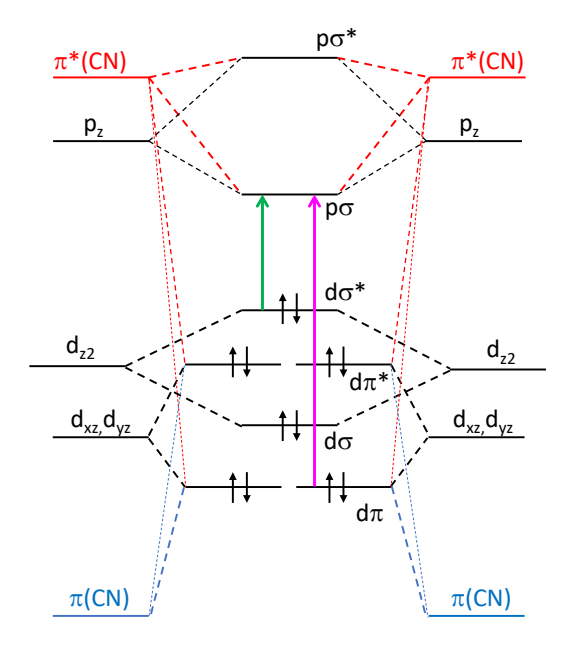
Abstract

Binuclear Rh(I) and Ir(I) TMB (2,5-dimethyl-2,5-diisocyanohexane) and dimen (1,8-diisocyanomenthane) complexes possess do*p σ and d π p σ singlet and triplet excited states that can be selectively excited in the visible and UV spectral regions. Using perturbational spin-orbit TDDFT, we unraveled the detailed character and spin-mixing of these electronic transitions and found that delocalization of p σ and d π orbitals over C=N-groups makes C=N stretching vibrations sensitive reporters of electron-density and structural changes upon electronic excitation. Picosecond time-resolved infrared (TRIR) spectra measured after visible, 375-, and 316-nm excitation revealed excitation-wavelength-dependent deactivation cascades. Visible-light irradiation prepares the 1 d σ *p σ state that, after one or two (sub)picosecond relaxation steps, undergoes 70-1300 ps intersystem crossing to 3 d σ *p σ , which is faster for the more flexible dimen complexes. UV-excited 1,3 d π p σ states decay with (sub)picosecond kinetics through a manifold of

high-lying triplet and mixed-spin states to ${}^3\text{d}\sigma^*p\sigma$ with lifetimes in the range 6-19 ps (316 nm) and 19-43 ps (375 nm, Ir only), bypassing ${}^1\text{d}\sigma^*p\sigma$. Most excited-state-conversion and some relaxation steps are accompanied by direct decay to the ground state that is especially pronounced for the most flexible long/eclipsed Rh(dimen) conformer.

INTRODUCTION

Binuclear complexes of $4d^8$ and $5d^8$ metals (Rh^I, Pt^{II}, Ir^I) exhibit greatly strengthened metal-metal bonds in low-lying electronic excited states. This bond strengthening is attributable to their unique electronic structure (Scheme I): the HOMO is a σ -antibonding combination of two $(n-1)d_{22}$ orbitals ($d\sigma^*$) and the LUMO is a σ -bonding combination of two np_z orbitals ($p\sigma$), with occupied $d\pi/\pi^*$ and $d\delta/\delta^*$ orbitals at lower energies. Excited-state metal-metal bonding was first proposed for [Rh(C \equiv N=Ph) $_4$] $^+$, which spontaneously dimerizes in solution. This discovery opened the way for research on bridged complexes with di-isocyano ligands (Figure 1) as well as on [Pt $_2$ (P $_2$ O $_5$ H $_2$) $_4$] $^{4-}$ (Pt(pop)) and its perfluoroborated derivative [Pt $_2$ (P $_2$ O $_5$ (BF $_2$) $_2$) $_4$] $^{4-}$ (Pt(pop-BF $_2$)).



Scheme 1. Qualitative MO diagram and principal spectroscopic transitions of d^8d^8 di-isocyanide complexes. Orbitals are described by their symmetry relative to M–M. The p σ LUMO is ca. 25% metal and 70% $\pi^*(C\equiv N)$. Metal character prevails in d σ and d σ^* (>90% d_{z2}), as well as in d π and d π^* (70-80% d_{xz}, d_{yz}). The lowest d $\sigma^* \rightarrow p\sigma$ transition is predominantly MMLCT (metal-metal to ligand charge transfer). p σ delocalization over C $\equiv N-$ groups and an absence of high-lying occupied ligand-localized orbitals are electronic features of d⁸d⁸ di-isocyanides that distinguish them from Pt(pop) and Pt(pop-BF₂),³ as well as Pt(pyrazolato)₂(ppy)₂ and related complexes.^{4, 5}

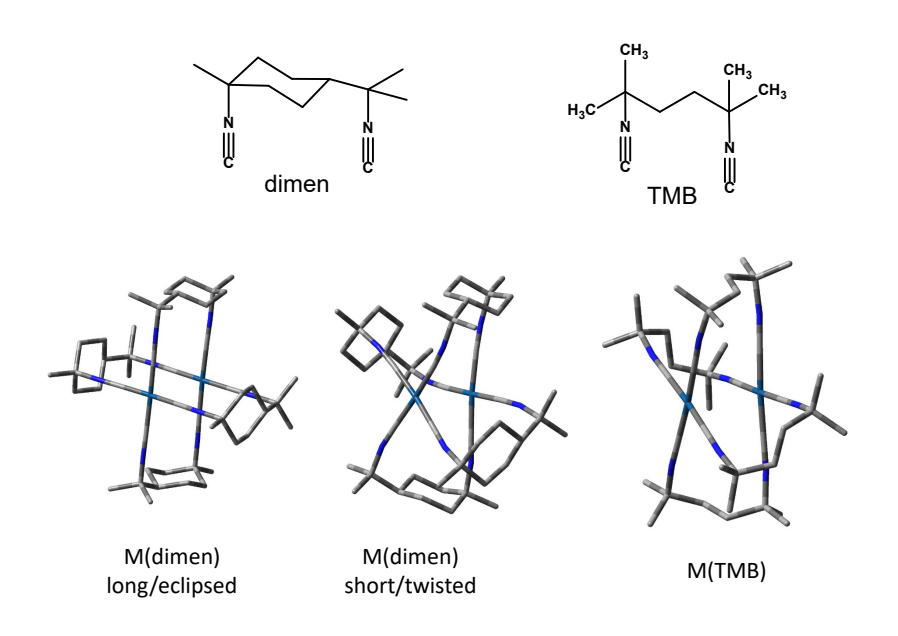


Figure 1. Top: Dimen (1,8-diisocyanomenthane) and TMB (2,5-dimethyl-2,5-diisocyanohexane) ligands. Bottom: Long/eclipsed and short/twisted conformations of the *trans*-2:2 [M_2 (dimen)₄]²⁺ isomer and the most stable [M_2 (TMB)₄]²⁺ conformer. The complexes are abbreviated M(dimen) and M(TMB), respectively. Structures were calculated for M = Ir.

The lowest electronic transition (green arrow in Scheme 1) generates a singlet 1 do*po excited state that undergoes relatively slow intersystem crossing to the corresponding 3 do*po triplet whose lifetime in di-isocyanide complexes varies from about 500 ps (Rh(dimen)⁶) to 400 ns (Ir(dimen)⁷), and is 10 µs for Pt(pop) and Pt(pop-BF₂).⁸ Exciting an electron from do* to po shortens the M–M distance, as determined for Pt(pop)⁹⁻¹² and Ir(dimen)^{13, 14} in time-resolved X-ray experiments. In the case of di-isocyanides, the excited po electron is largely delocalized over the C=N– groups (Scheme 1), thereby decreasing the ν (C=N) stretching frequency and opening the way for photophysical characterization by time-resolved IR spectroscopy (TRIR).^{15, 16}

Di-isocyanide complexes, as well as Pt(pop) and Pt(pop-BF2), behave as encaged M–M heavy-atom oscillators that are largely shielded from the medium, except for the outer molecular planes. Impulsive $d\sigma^* \rightarrow p\sigma$ excitation with femtosecond laser pulses creates M–M vibrational wavepackets whose coherent oscillations were observed in Pt(pop)¹⁷⁻¹⁹ and Ir(dimen)⁷ during the first few picoseconds after laser-pulse excitation. For Ir(dimen), we observed oscillation of the excited-state v(C=N) IR band width with the Ir–Ir stretching frequency during the first 1-2 ps, indicating that high-frequency v(C=N) vibrational modes are affected by the initial position of the slowly moving v(Ir-Ir) wavepacket. Of special interest is that experimental v(Ir-Ir) and theoretical v(Ir-Ir) investigations of vibrational energy dissipation following v(Ir-Ir) are excitation revealed different coherence dephasing mechanisms in Pt(pop) and Ir(dimen), intramolecular and stochastic, respectively. Stochastic Ir(dimen) dephasing can be related to the flexibility of the

dimen ligand, enabling phase changes as the wavepacket evolves across a range of configurations as well as frequent collisions with more strongly interacting solvent molecules at outer molecular planes. This finding supports the suggestion based on time-resolved X-ray scattering and QM/MM simulations¹⁴ that Ir(dimen) excitation is followed by subpicosecond desolvation and picosecond CH₃CN N-atom re-coordination. Remarkably, whereas most of the electronic and vibrational dynamics in d⁸d⁸ complexes are centered in the encaged M–M unit, excited-state chemistry and photocatalysis (hydrogen abstraction, ²²⁻²⁴ dehydrogenation, ²⁵ atom transfer, ²⁶⁻²⁸ H₂ evolution^{29, 30}) occur at outer molecular planes, owing to electron density redistribution and the radical character of ³do*po states. ²²

In addition to the ${}^{1}\text{d}\sigma^{*}\to p\sigma$ system in the visible region, absorption spectra of ${}^{8}\text{d}^{8}$ disocyanides exhibit one (Rh) or two (Ir) sharp UV bands (Figure 2) attributable to singlet and triplet ${}^{4}\text{d}\pi\to p\sigma$ transitions. ${}^{6,\ 31,\ 32}$ The presence of several well-defined and spectrally isolated absorption features provides an opportunity to investigate deactivation pathways as well as electronic and vibrational energy channels that are triggered by populating different initial excited states. To this end, after selectively exciting ${}^{1}\text{d}\sigma^{*}\to p\sigma$, ${}^{1}\text{d}\pi\to p\sigma$, and ${}^{3}\text{d}\pi\to p\sigma$ transitions of M(TMB) and M(dimen) complexes (M = Rh, Ir; Figure 1), we followed the ensuing excited-state dynamics using TRIR spectroscopy and characterized excited-state electronic structures by perturbational spin-orbit TDDFT calculations. TMB complexes were chosen because their ground-state structures feature rather short M–M distances and two M(C=N-)4 planes twisted relative to each other as in ${}^{4}\text{d}\sigma^{*}$ excited states. With Ir(dimen), we studied two conformations with short and long Ir–Ir distances (short/twisted and long/eclipsed) that could be selectively excited

in the visible (but not the UV) region. Comparison with Rh(dimen) is of special interest, as it is structurally more flexible.⁶

In our work, we have fully characterized the ground-state structures, relevant vibrational modes, and electronic transitions of the four complexes. We also have investigated the ultrafast evolution of IR spectra upon optical excitation across the UV-vis spectral range. Of importance is our finding that the lowest 3 do*po state is populated directly from higher electronic states whose decay largely bypasses the lowest 1 do*po state and often is accompanied by a partial conversion to the ground state. Although on a (sub)picosecond timescale, relaxation of UV-populated states is considerably slower than in mononuclear metal complexes featuring ligand- and metal-centered and metal-to-ligand charge transfer excited states.

RESULTS AND DISCUSSION

The complexes $[M_2(TMB)_4](TFPB)_2$ and $[M_2(dimen)_4](TFPB)_2$ (M = Rh, Ir; TFPB = tetrakis[3,5-bis(trifluoromethyl)phenyl]borate) were investigated in degassed flowing MeCN solutions by IR spectra measured at selected time delays after ~50 fs laser pulse excitation in the $v(C\equiv N)$ region. Structures and $v(C\equiv N)$ vibrations were calculated by DFT using a PBEO functional. Perturbational spin-orbit TDDFT (pSOC-TDDFT)^{34, 35} was used to calculate and analyze electronic transitions. For experimental and computational details, see section S12 in the SI.

Ground-state structures and C=N vibrations. M(TMB) conformations differ in the folding of the $-(CH_2)_2-$ link between the isocyanide groups of individual ligands. DFT calculations of both complexes in MeCN indicated the predominant presence of a single conformation with a metal-

metal distance of 3.32 Å for Rh and 3.16 Å for Ir, in agreement with crystallographic values (3.262 and 3.119 Å, respectively). 36-38 The two M(C≡N−)4 planes are twisted relative to each other by 28°. Other calculated conformations had similar M-M distances and were at least 0.21 (Rh) and 0.11 eV (Ir) higher in energy (Table S1). In the most stable conformation, all four TMB ligands are folded in the same way (Figure 1) and the structure has approximately D₄ symmetry. The asymmetry of the dimen ligand gives rise to several M(dimen) orientational isomers that differ by relative head-to-tail orientations of the four dimen ligands (Tables S2, S3). Since the calculated electronic structures and $v(C \equiv N)$ vibrations are virtually identical for different isomers, we base further discussion on the most symmetrical one, trans-2:2 (Figures 1 and S1-left). More importantly, M(dimen) occurs in two conformations with markedly different M-M distances and twist angles, known as "short/twisted" and "long/eclipsed", which have different spectroscopic and photophysical properties.^{6, 7, 16, 36, 39} In fluid solution, these conformations occur simultaneously in a temperature-dependent equilibrium.³⁹ Two energetic minima were found by DFT, corresponding to short/twisted and long/eclipsed conformers for each Ir(dimen) orientational isomer with Ir-Ir distances (twist angles) in the ranges 3.25-3.38 Å (38.4-39.4°) and 4.16-4.34 Å (8.9-0°), respectively (Table S2). The presence of two distinct conformations in a MeCN solution was confirmed by X-ray scattering¹³ that estimated the Ir-Ir distances as 3.6 and 4.3 Å as well as by the observation⁷ of v(Ir-Ir) vibrational frequencies of 48 and 11 cm⁻¹. For Rh(dimen), a shallow ground-state potential energy surface was proposed based on the shape of its electronic absorption spectrum⁶ along with structural modeling.³⁹ In agreement, there were several minima in r(Rh-Rh)/twist angle space (Table S3), indicating a rugged potential energy surface and a broad conformational distribution. For the trans-2:2 orientational isomer, the long/eclipsed (Rh–Rh = 4.24 Å, 0° twist) conformation had the lowest energy; and a short/twisted conformation (3.36 Å, 38.1°) and at least one intermediate form (3.98 Å, 25.4°) were calculated at slightly higher energies (0.1, 0.02 eV).

There is a single intense band in the ground-state IR spectrum of each complex in the v(C=N) region [2157 cm⁻¹ (lr); 2163-2166 cm⁻¹ (Rh)] (Figure S2, Table S4). Each band is accompanied by a very weak feature at 2200-2210 cm⁻¹. The M(TMB) v(C≡N) band was best fitted by one strong Lorentzian, plus a very weak one that contributed to its high-energy side. The 2200–2210 cm⁻¹ feature is very weak in M(dimen) spectra but more prominent for Rh(TMB) and, especially, Ir(TMB). Harmonic DFT vibrational analysis indicated that the $v(C \equiv N)$ modes follow a D_4 pattern: $A_1 \oplus A_2 \oplus B_1 \oplus B_2 \oplus 2E$. Calculated wavenumbers and intensities are summarized in Tables S5-S8; and corresponding C≡N stretching motions are displayed in Figure S3. The principal IR band corresponds to one of the E modes (bE in Tables S5-S8) that splits to quasidegenerate $bB_2 \oplus bB_3$ modes in D_2 symmetry. Their quasidegeneracy was retained (within 1 cm⁻¹) when no symmetry was imposed in the calculations. The second $aB_2 \oplus aB_3$ (D_2) set arising from the aE mode (D_4) is at similar energies (≤ 6 cm⁻¹) as the bE set but with lower intensities. The two sets were not distinguished in the experimental spectra. The weak 2200-2210 cm⁻¹ feature is attributable to the bB_1 (D_2) vibration of an A_2 origin in D_4 . (Individual vibrations are denoted by their D_2 and D_4 -parent symmetries as $D_2(D_4)$, see also Tables S5-S8.) The $bB_2(bE)$ and $bB_3(bE)$ modes of M(dimen) were calculated to fall 14 (Ir) and 12 (Rh) cm⁻¹ higher for the long/eclipsed than for the short/twisted conformations. Accordingly, the two Lorentzians constituting the strong IR band (red and blue in Figure S2-top, split by 7 and 5 cm⁻¹) are attributed to these two conformations. By analogy, the weak low-energy feature in M(TMB) spectra (green in Figure S2-bottom) likely belongs to one of the minor conformers.

All $v(C\equiv N)$ vibrations of the lowest ${}^3d\sigma^*p\sigma$ state were calculated at lower wavenumbers than their ground-state counterpart (Tables S5-S8). The most IR-intense modes $bB_2(bE)$ and $bB_3(bE)$ shift downwards by 10-18 cm⁻¹. A similar shift was calculated for $aB_3(aE)$, which also gains intensity. The largest effect was calculated for $bB_1(A_2)$, which shifts to lower wavenumbers by ca. 60 (Ir) and 80 (Rh) cm⁻¹ while gaining intensity, especially for Rh. This mode corresponds to a symmetrical $v(C\equiv N)$ vibration of each of the two $M(C\equiv N-)_4$ planes that vibrate in opposite phases (Figure S3).

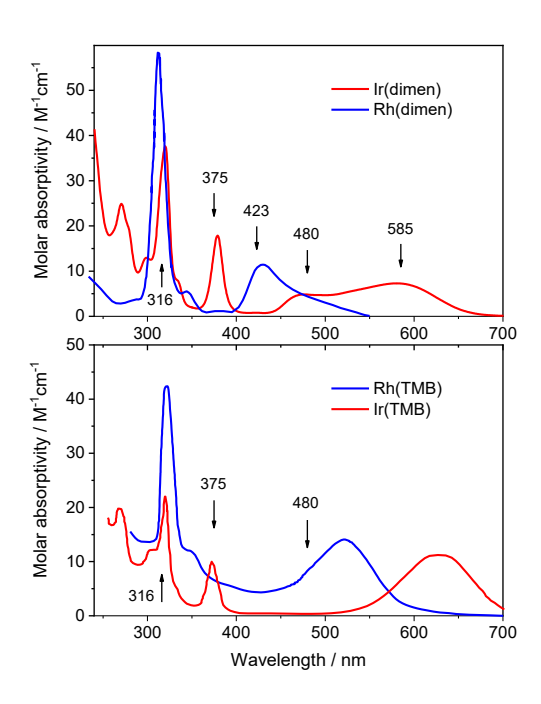


Figure 2. UV-vis absorption spectra of M(dimen) and M(TMB) complexes in MeCN solution. Molar absorptivities taken from the literature. ^{31, 32, 36} Data for Rh(dimen) and M(TMB) taken from earlier work. ^{6, 38, 40} The arrows show excitation wavelengths used in TRIR experiments, values in nm.

Electronic transitions. The electronic absorption spectrum of each of the d⁸d⁸ di-isocyanide complexes features an intense visible band whose shape and energy are strongly structure-

dependent, and there also is a strong UV band between 314 and 320 nm (Figure 2). The Ir complexes exhibit an additional UV band in the 372-378 nm region. Notably, pSOC-TDDFT calculations accord with previous assignments of these bands (Tables S9–S26).^{1, 6, 16, 31, 39}

The electronic transition responsible for the visible absorption band was found to have nearly 100% d $\sigma^* \rightarrow p\sigma$ spin-singlet character. The triplet contribution amounts to 1% (Rh) and 3% (Ir); and the ${}^{1}\text{d}\sigma^{*} \rightarrow p\sigma$ band occurs at 517 nm (Rh(TMB)) and 625 nm (Ir(TMB)). 31 Of interest are the two visible systems in the spectra of dimen complexes attributable to short/twisted (590 nm (Ir), 450-550 nm shoulder (Rh)) and long/eclipsed (480 nm (Ir), 423 nm (Rh)) conformers.^{6, 7, 16, 36,} 39,41 The do* HOMO in all four complexes is $^{\sim}90\%$ metal-localized, whereas the po LUMO is highly delocalized over the C=N- groups (about 25% metal p_z and 70% CN π^*), imparting substantial MMLCT (metal-metal to ligand charge transfer) character to 1 d σ^{*} p σ , as well as to the lowest triplet ${}^{3}d\sigma^{*}p\sigma$ (${}^{3}A_{2}$) state, whose bA₁ and aE spin-orbit components are $\geq 95\%$ ${}^{3}d\sigma^{*}\rightarrow p\sigma$. It follows that the well-established strengthening/shortening of the M–M interaction upon singlet or triplet $d\sigma^* \rightarrow p\sigma$ excitation originates from $d\sigma^*$ depopulation and $p\sigma$ population, $^{1, 6, 7, 13, 14, 42-44}$ the latter associated with partial po bonding and strengthening $\pi\pi$ and dispersive interactions between the M(C=N-)₄ planes. Notably, both do*po singlet and triplet contain a ${}^3d\pi p\sigma$ admixture that is larger for Ir than Rh and, in M(dimen), for long/eclipsed rather than short/twisted conformations. Mixing with 3 d π p σ amounts to second-order SOC between singlet and triplet d σ *p σ states and likely enables ${}^{1}d\sigma^{*}p\sigma \rightarrow {}^{3}d\sigma^{*}p\sigma$ ISC.

In accord with the original assignment,^{6, 31} TDDFT calculations found that the $d\pi(d_{xz},d_{yz})\to p\sigma$ transition is responsible for the intense 314-320 nm band. The ${}^1d\pi(d_{xz},d_{yz})\to p\sigma$ excitation contributed 95% to the band intensity of each of the Rh complexes, while there was

extensive mixing among ${}^1d\pi(d_{xz},d_{yz})\to p\sigma$, ${}^3d\pi(d_{xz},d_{yz})\to p\sigma$, ${}^3d\pi^*(d_{xz},d_{yz})\to p\sigma^*$, and ${}^3d\delta/d\delta^*(d_{xy})\to p\sigma$ excitations in each of the Ir isocyanides. The calculated ${}^1d\pi\to p\sigma$ contribution decreased from 76 to 65, and to 54% on going from long/eclipsed to short/twisted Ir(dimen), and to Ir(TMB). Both Ir complexes exhibited an additional UV band (372-378 nm) attributable to a mixed-spin transition (${}^{\sim}85\%^3d\pi\to p\sigma$ with ${}^{\sim}10\%^1d\pi\to p\sigma$). This band is the triplet counterpart of the stronger 314-320 nm system. The singlet contribution drops to about 2% in each of the Rh complexes, accounting for a weak shoulder observed 31 at about 340 nm. The $d\pi$ orbital mixes 70-76% $d_{xz}+d_{yz}$ character mostly with C=N π -bonding orbitals (Scheme 1). It follows that both 314-320 and 372-378 nm $d\pi\to p\sigma$ excitations have a partial $\pi\to \pi^*$ character, weakening C=N bonds more than $d\sigma^*\to p\sigma$ excitations, in agreement with calculated bond orders and electron-density redistribution (Table S28 and Figure S35, SI section 11). M–M distances are expected to shrink in $d\pi p\sigma$ excited states, but less than in $d\sigma^*p\sigma$ ones.

Excitation-wavelength-dependent photophysics. TRIR spectra in the $v(C\equiv N)$ region were measured following excitation in the visible range ($^1\text{d}\sigma^* \rightarrow p\sigma$), at 375 nm ($^3\text{d}\pi \rightarrow p\sigma$, Ir only), and at 316 nm ($^1\text{d}\pi \rightarrow p\sigma$ (Rh), $^1\text{d}\pi \rightarrow p\sigma$ plus triplet contributions for Ir). Two different visible excitation wavelengths were used for M(dimen), allowing separate study of long/eclipsed and short/twisted conformers. Note that both conformers absorb in the UV at virtually identical wavelengths (Figure 2), although calculated oscillator strengths indicated preferential absorption by the long/eclipsed conformer.

Time-evolution of $v(C\equiv N)$ IR absorption is depicted as TRIR 2D color maps in Figures 3 and 4; and raw TRIR spectra are shown in Figures S5-S8. TRIR signals consisted of a negative band due

to the depleted GS population (bleach) and a broad positive excited-state absorption (ESA) at lower wavenumbers. The high-energy side of the ESA band overlapped with the bleach. An additional weak bleach was apparent at about 2200-2210 cm $^{-1}$, becoming more pronounced in the case of Ir(TMB). A very weak time-dependent signal at 2240-2250 cm $^{-1}$ is attributable to acetonitrile $v(N\equiv C)$ absorption.

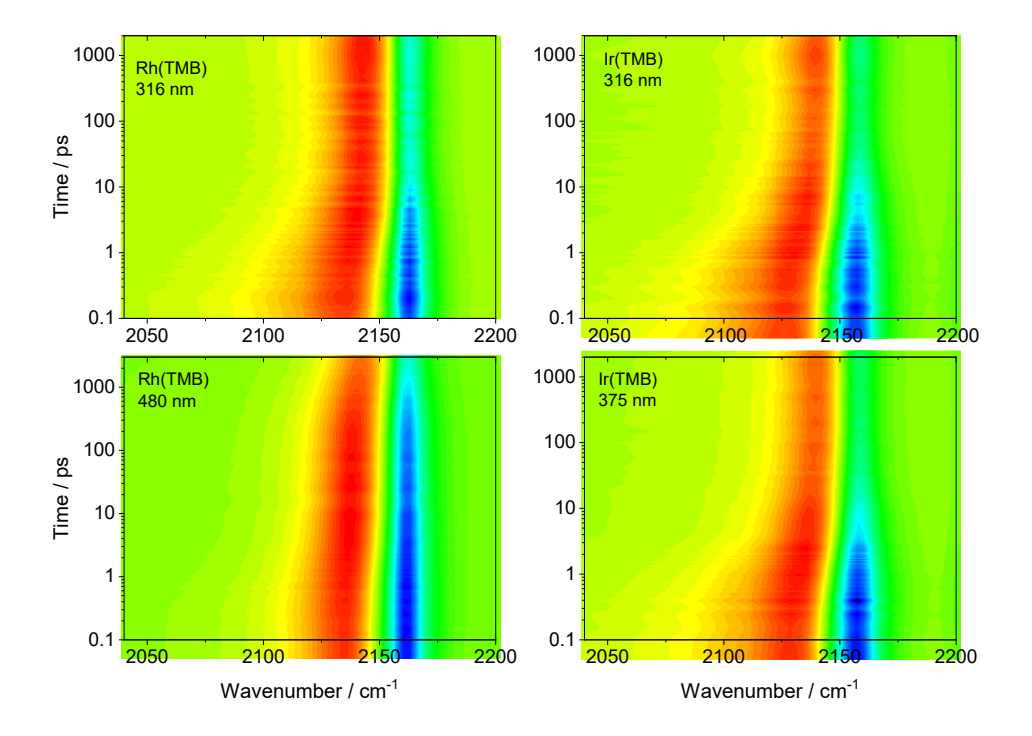


Figure 3. Time evolution of IR absorption of Rh(TMB) and Ir(TMB) after ~50 fs laser pulse excitation at different wavelengths. TRIR spectra are shown as time-wavenumber 2D plots, positive signal in red, negative (bleach) in blue.

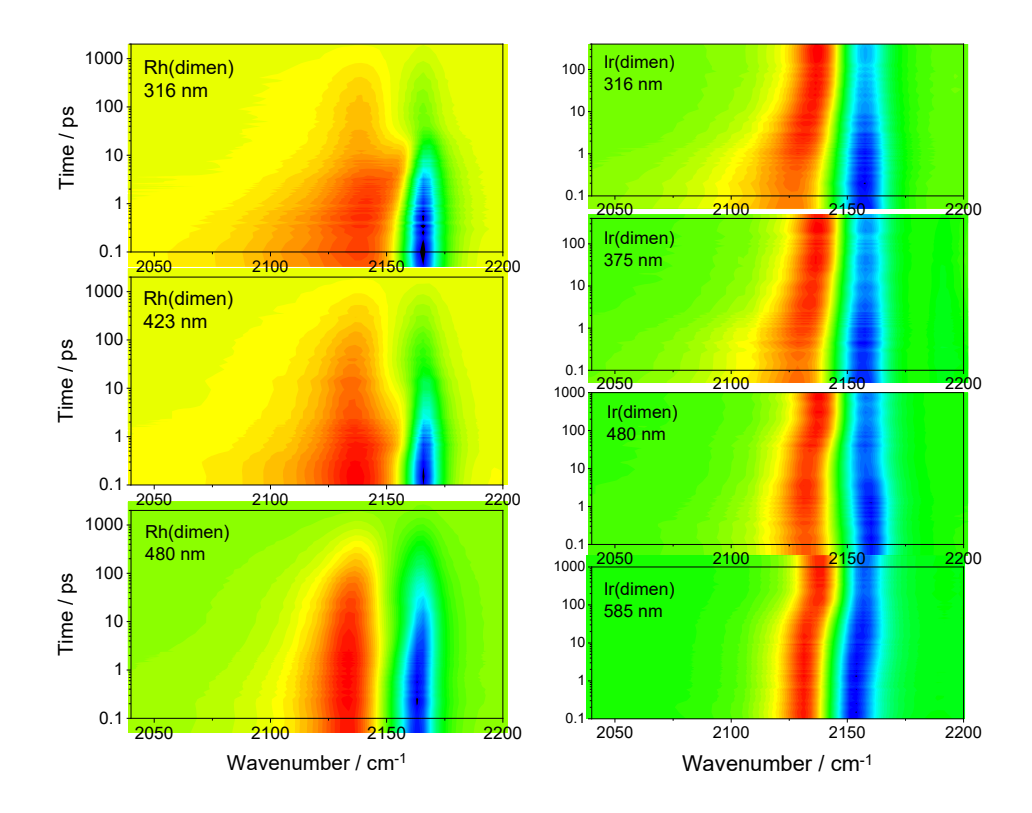


Figure 4. Time evolution of IR absorption of Rh(dimen) and Ir(dimen) after $^{\sim}50$ fs laser pulse excitation at different wavelengths. TRIR spectra are shown as time-wavenumber 2D plots, positive signal in red, negative (bleach) in blue. [The Ir(dimen) data at 585 nm were taken from earlier work¹⁶ with wavenumbers shifted by -2.5 cm⁻¹ to account for differences in instrument calibration.]

TRIR spectral evolution consisted of several steps, each accompanied by an ESA shift, narrowing, and intensity changes, as well as a partial bleach area decay, whose magnitudes and timings depended on the complex and excitation wavelength. TRIR dynamics upon visible excitation has been studied in detail for Ir(dimen). Its last step involved an ESA upshift caused by $^{1}\text{d}\sigma^{*}p\sigma \rightarrow ^{3}\text{d}\sigma^{*}p\sigma$ intersystem crossing (ISC). (It is clearly visible as a kink in 585 and 480 nm Ir(dimen) TRIR 2D maps around 70 ps, Figure 4-right.) By analogy, we assumed that visible excitation of all investigated complexes eventually populates the lowest relaxed $^{1}\text{d}\sigma^{*}p\sigma$ state that undergoes ISC to the lowest triplet, $^{3}\text{d}\sigma^{*}p\sigma$. [In support, the TRIR lifetime associated with

the last kinetics step for Rh(TMB), 891 ps, accords with the reported³² fluorescence lifetime of 900 ps.] Moving the excitation wavelength to the UV region did not change this general TRIR pattern, although there were several important differences: (i) initial ESA occurred at lower wavenumbers upon shorter-wavelength excitation, whereas the final spectra (attributed to relaxed 3 do*po) were independent of the excitation wavelength; (ii) initial ESA was broader upon shorter-wavelength excitation, and the initial dynamic narrowing was more prominent; (iii) exciting at shorter wavelengths accelerated the ESA upshift attributable to the 3 do*po population; and (iv) with 423 or 316 nm excitation, Rh(dimen) exhibited an extra transient feature peaking between the principal ESA and the bleach.

Time- and excitation-wavelength dependent $v(C\equiv N)$ IR spectra contain information on dynamics and deactivation mechanisms of different electronic excited states. Relevant here is that DFT vibrational analysis indicated the presence of two or three closely spaced contributing excited-state vibrations ($bB_2(bE)$, $bB_3(bE)$, and weaker $aB_3(aE)$), plus the $bB_1(A_2)$ mode that gains intensity upon excitation and shifts down to the region of the bleach or even lower (Tables S5-S8). Time-dependent ESA narrowing, shifts, and intensity changes could originate from vibrational relaxation (IVR, VR, structural changes) as well as from conversions between different electronic states. As small magnitudes of spectral changes in combination with large bandwidths often obscured differences between dynamic IR band shifts and changing spectral patterns, we based interpretation of TRIR spectra on kinetics and shape fitting. We employed complementary approaches that yielded similar results: (i) global kinetics fitting of time-dependent intensities (Δ Abs) across the whole spectrum to sums of exponentials. In this way, the spectral evolution was reduced to 3-5 kinetics steps i, each characterized by an exponential lifetime τ_i and an

evolution-associated (EA_i) spectrum that described the system at the onset of the step i (and at the completion of step i-1). [EA_i spectra were calculated using the sequential kinetics model. EA₁ is the TRIR spectrum extrapolated to t = 0 that approximately corresponds to the Franck-Condon (FC) optically excited state. The last EA_i spectrum is attributable to the lowest ${}^3d\sigma^*p\sigma$ state.] To determine spectral parameters at individual reaction stages, the shapes of EA_i spectra were fitted by one negative Lorentzian whose peak wavenumber and width were fixed at GS values taken from the FTIR spectrum, and one or two positive Lorentzian ESA peaks. [The number and shapes of ESA peaks were determined by comparing fits with different input parameters. Gaussian bandshapes did not match the spectra. For Ir(TMB), the ~2200 cm⁻¹ feature was also included in the fits.]; (ii) raw-spectra shape-fitting, whereby TRIR spectra obtained at each delay time were fitted to a fixed negative GS bleach and one or two ESA Lorentzians. This procedure provided time evolution of ESA peak wavenumbers, bandwidths, and bleach areas whose kinetics were fitted by sums of exponentials. ESA wavenumbers extrapolated to zero and infinity times closely matched ESA peaks in the first and last EA spectra. Lifetimes were similar to those obtained by global fitting, albeit with larger uncertainties. Note that Rh(dimen) raw-spectra analysis revealed a slow relaxation step missed by global fitting.

Next we describe and interpret TRIR evolution to shed light on excited-state relaxation and decay mechanisms for the four complexes (Schemes 2 and 3). Lifetimes determined by global kinetics analysis are summarized in Tables 1 and S27. Detailed spectral analysis is presented in sections 6-9 of the SI.

Table 1. Lifetimes and bleach recovery yields of TRIR kinetics steps at different excitation wavelengths. Determined by global kinetics analysis of TRIR spectra.^a

Complex	Excitation	Globally fitted lifetimes in ps				³dσ*pσ
	wavelength	(Estimated GS recovery yield, %) ^b				lifetime ^c
					³dσ*pσ	
					population	
Rh(TMB)	480 nm		1.43 (3)	6.1 (8)	891 (30)	30 ns
	316 nm ^d		1.25 (0)	5.9 (31)	~1300 (0)	30 ns
	316 nm ^e		1.19 (0)	-	5.7 (30)	30 ns
Ir(TMB)	375 nm		1.14 (0 ^f)	2.23 (28)	34 (23)	100 ns
	316 nm		0.80 (<2)	1.31 (13)	19.1 (30)	100 ns
Ir(dimen)	585 nm			5.42 (~0)	73.0 (~0)	300 ns
	480 nm		0.35 (16)	4.9 (36)	72 (0)	300 ns
	375 nm ^f		0.77 (≤4)	2.2 (16)	43 (≤4)	300 ns
	316 nm		0.76 (0)	1.67 (19)	21.1 (10)	300 ns
Rh(dimen)	480 nm			2.41 (≤10)	36.1 (47)	497ps ^g
	423 nm	0.09 ^h (0)	0.46 (0)	1.71 (≤44)	19.6 (60)	500 ps
	316 nm	0.22 (5%)	0.94	5.1	12.9 (~85)	500 ps ⁱ

^a Lifetimes with \pm errors are summarized in Table S27. ^b Calculated from EA_{i-1} and EA_i integrated bleach areas. ^c Values in this column were taken from the literature and fixed in global analysis except the 497/500 ps Rh(dimen) lifetime, which we determined by TRIR. ^d 4-exponential fit. ^e 3-exponential fit. ^f Spectral region above 2180 cm⁻¹ was discarded from the global fit to avoid any effects of photoproduct dynamics (Figure S7). ^g Free fit of data measured to 3 ns. ^h The lifetime value provided by the global fit is shorter than the instrument time resolution, ca. 0.15 ps. ⁱ Free fit of data measured to 2 ns gave a value of 630 ps.

Rh(TMB). Perusal of TRIR 2D maps and spectra (Figures 3, S5) indicates two time ranges where the ESA signal shifted to higher wavenumbers after 480 nm (1 d $\sigma^{*} \rightarrow p\sigma$) excitation: 1-10 and 600-1000 ps. The initial signal after 316 nm (1 d $\pi^{*} \rightarrow p\sigma$) excitation was much broader and its evolution was essentially complete at 10-20 ps when the spectrum closely resembled that for 480-nm excitation taken at long time delays (>2000 ps).

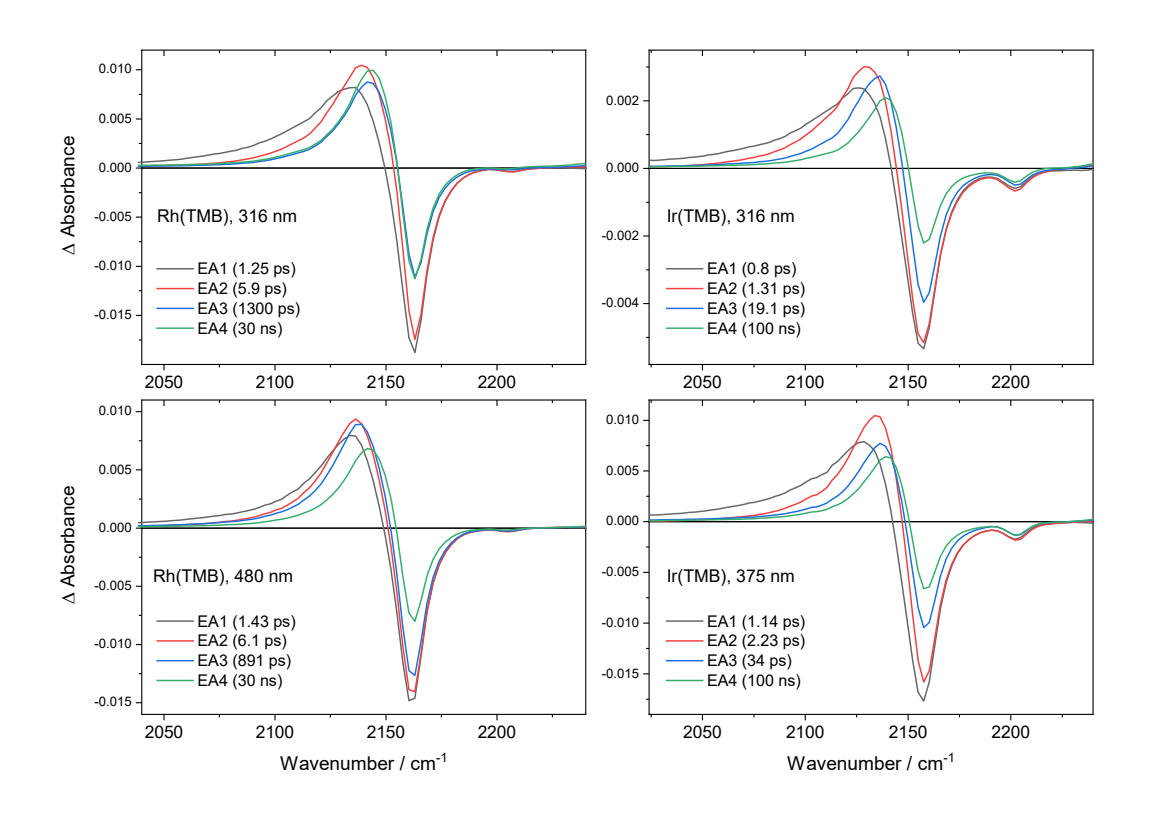


Figure 5. Evolution-associated (EA_i) spectra obtained by global kinetics analysis of Rh(TMB) and Ir(TMB) TRIR spectra. Corresponding lifetimes in parenthesis (τ_i). The spectra evolve in the direction black \rightarrow red \rightarrow blue \rightarrow green. The black spectra are extrapolated to t=0 and correspond to Franck-Condon states excited at given wavelengths. The green spectra are attributable to the lowest triplet, ${}^3\text{d}\sigma^*\text{p}\sigma$. The blue spectrum in the bottom-left panel corresponds to the lowest ${}^1\text{d}\sigma^*\text{p}\sigma$ state of Rh(TMB). Lorentzian shape-fits and spectral parameters are displayed in Figures S9-S12 (Rh) and S16-S17 (Ir).

Global kinetics fitting of 480-nm-excited TRIR spectra revealed three kinetics steps with lifetimes of 1.43, 6.1, and 891 ps (Figures 5, S9, S10). The spectral time evolution started with ESA (EA_1) at 2132.7 cm⁻¹ and finished with a long-lived signal (EA_4) at 2143.6 cm⁻¹ attributable to the lowest 3 d σ^* p σ state. Its lifetime was fixed at 30 ns from published 32 phosphorescence decay data. As the lifetime of the preceding step, 891 ps, matched the reported 32 1 d σ^* p σ fluorescence decay lifetime (900 ps), the corresponding EA_3 spectrum (2138.4 cm⁻¹) was assigned to the relaxed 1 d σ^* p σ state. The first two steps (1.43 and 6.1 ps) are attributable to relaxation of the

optically excited Franck-Condon (FC) ¹dσ*pσ state, which involves 0.46 Å Rh–Rh bond contraction (DFT-calculated), adjustments in the geometry of TMB bridges, solvent restructuring, and vibrational cooling. These changes were accompanied by small upshifts (+3.5, +2.2 cm⁻¹) and narrowing (-2.9, -0.9 cm⁻¹) of the fitted Lorentzian ESA peak. The 891-ps ISC to 3 d σ^* p σ involves a larger (+5.2 cm⁻¹) shift and virtually no narrowing (Figure S9). A more detailed analysis of EA_i spectral shapes (Figure S10) revealed the presence of two contributing peaks that both shifted to higher wavenumbers, while the higher lying one lost intensity with time. These peaks are attributed to different v(C≡N) modes (DFT calculations, Table S8). The "moving band" (green in Figure S10) presumably corresponds to the bB₁(A₂) vibration calculated to occur 24 cm⁻¹ lower in the 3 do*po state than in GS (expt. -14 cm $^{-1}$, Figure S10). The 6.1 and 891 ps steps also involved a decrease of the bleach band area by ca. 8 and 30%, respectively (Figures S9, S10, and apparent in the 2D map, Figure 3) that could be caused by GS recovery and/or by increasing overlap with an unidentified positive ESA that could occur in the bleach region. Since neither EAi and rawspectra shape fits nor DFT indicated a significant presence of such an ESA, the bleach decay was attributed to GS recovery.

Excitation at 316 nm produced an initial signal (EA_1) at 2133.4 cm⁻¹ that was much broader than that employing 480 nm (Figures 3, S5, S11, S12); its time evolution was globally fitted with a 4-exponential function (Figure 5, EA_i parameters in Figures S11, S12). The first kinetics step (1.25 ps) was accompanied by a large ESA upshift (+8.3 cm⁻¹) and narrowing that indicated conversion to lower-lying electronic states. As the resulting ESA (EA_2) was distinctly *above* any of the intermediate spectra observed upon 480-nm excitation, we concluded that 1 d σ^* p σ was not significantly populated during UV-excited 1 d π^* p σ decay. In the next step (5.9 ps), a spectrum

(EA₃) attributable to 3 d σ^{*} p σ was observed. Except for a small rise in intensity (3.7%), this spectrum is virtually identical to EA4 obtained after the 1300±370-ps step. These observations suggest that ³dσ*pσ is populated by two parallel pathways: an ultrafast (5.9 ps) channel from higher lying intermediate electronic states bypassing ${}^{1}d\sigma^{*}p\sigma$; and by a slow "conventional" route through ¹dσ*pσ. The latter pathway contributes very little, as was evidenced by the very small difference between EA₃ and EA₄ ESA areas (Figure 5), a large uncertainty of the 1.3 ns lifetime (±30%, in contrast to <2.5% for the two faster lifetimes), and a small preexponential factor across the TRIR range (Figure S13). Notably, by omitting the 1.3 ns step, we obtained a statistically equivalent 3-exponential fit (1.19, 5.70 ps, 30 ns), where the EA₃ spectrum of ³dσ*pσ was fully formed in the 5.70 ps step (Figures S13, S14) and its immediate precursor spectrum differed from that of 1 d σ^{*} p σ after 480-nm excitation. The absence of both the ${}^{\sim}$ 900-ps kinetics step and a 1 do*po spectral feature supported the above conclusion that the lowest (relaxed) excited singlet is largely bypassed during ${}^{1}d\pi^{*}p\sigma$ decay; and this conclusion agrees with the diminished relative intensity of the 316 nm band in the fluorescence excitation spectrum.³² Parallel to populating 3 d σ^{*} p σ , the 5.9 ps (or 5.7 ps) step also involves $^{\sim}$ 30% bleach recovery.

The above conclusions based on global analysis and EA_i spectra were supported by TRIR spectral-parameter time dependences (Figure S15). The raw ESA peak wavenumber shifted upwards with lifetimes of 1.8, 11, and 1000 ps (480 nm excitation) and 1.2 and 5.0 ps (316 nm) to a limiting value of 2144–2145 cm⁻¹, attributable to ${}^3\text{d}\sigma^*\text{p}\sigma$. After 480-nm excitation, virtually all band narrowing took place in the fastest kinetics component, whereas biphasic narrowing was observed following 316 nm excitation: 1.0 ps (-9 cm^{-1}) plus 9 ps (-6 cm^{-1}). GS recovery yields estimated from the bleach-area decrease and from global analysis are very similar. Raw spectra

could also be fitted with two ESA Lorentzians, supporting contributions from two vibrational modes.

Work on Ir(TMB) revealed spin and composition effects on the optically excited $d\pi p\sigma$ states: 54% ($^{1}d\pi p\sigma$)+15% ($^{3}d\pi p\sigma$) + 27% ($^{3}d\delta^{*}p\sigma$) for 316 nm and 83% ($^{3}d\pi p\sigma$) + 10% ($^{1}d\pi p\sigma$) for 375 nm excitation (Table S9). In both cases, the initial signal (EA_1) was very broad (51, 55 cm⁻¹), peaking at different wavenumbers: 2131.2 cm⁻¹ (375 nm excitation) and 2128.4 cm⁻¹ (316 nm excitation) (Figures S16, S17). Global fitting revealed 3-exponential evolution toward a common long-lived feature at 2144.5 cm⁻¹ (31 cm⁻¹ fwhm) that likely corresponds to the lowest ³dσ*pσ state. All kinetics steps become faster on changing the excitation wavelength from 375 nm (1.14, 2.23, and 34 ps) to 316 nm (0.80, 1.31, and 19.1 ps). Since narrow bandwidths of both 375 and 316 nm absorption bands imply small distortions of 1,3 d π p σ states relative to the GS and make populating high vibrational levels unlikely, we attribute the first two steps to conversions into intermediate electronic state(s) and ensuing electronic, vibrational, and structural/solvational relaxation through the manifold of high-lying electronic states, in accord with 13-14 and 4-5 cm⁻¹ ¹ narrowing in the first and second steps at both excitation wavelengths. Both steps were accompanied by ESA upshifts. After 375-nm excitation, the larger shift (+7.7 cm⁻¹) occurred in the first step, whereas following 316 nm excitation, the larger shift (+6.7 cm⁻¹) was observed in the second step. In both cases the last step produced the same ³dσ*pσ state but with distinctly different kinetics: 34 ps (375 nm excitation) and 19.1 ps (316 nm excitation). The EA₃ spectra of its immediate precursor were different at 375 nm excitation (peak 2141.8 cm⁻¹; fwhm 34 cm⁻¹) and 316 nm excitation (2139.5; 36 cm⁻¹) (Figures S16, S17). These observations suggest that singlet and triplet $d\pi p\sigma$ states decay through different intermediate states and their deactivation

pathways converge only at the level of the ${}^3\text{d}\sigma^*p\sigma$ lowest triplet. The second and third steps at either excitation wavelength were accompanied by decreasing bleach intensity (Table 1, Figures S16, S17), indicating that up to 50% of the UV-excited population was lost by ultrafast decay to the ground state. The complementary raw-TRIR analysis is shown in Figure S18, supporting the above conclusions.

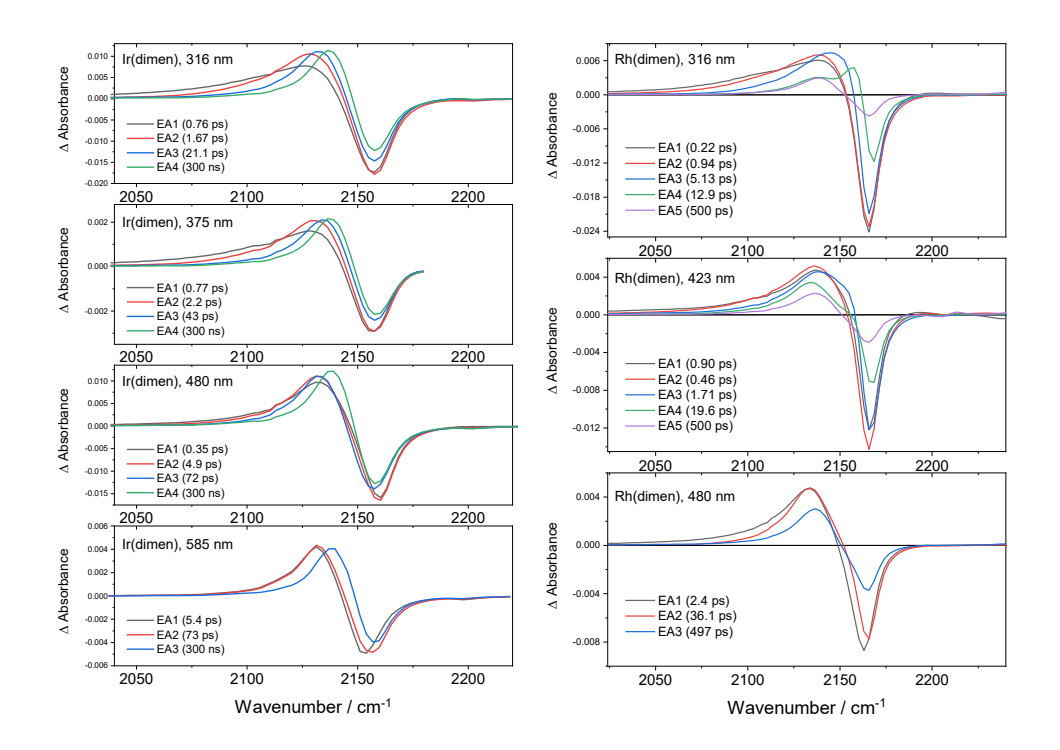


Figure 6. Evolution-associated (EA_i) spectra obtained by global kinetics analysis of Ir(dimen) and Rh(dimen) TRIR spectra. Corresponding lifetimes in parenthesis (τ_i). The spectra evolve in the direction black \rightarrow red \rightarrow blue \rightarrow green. The black spectra are extrapolated to t=0 and correspond to the Franck-Condon states excited at given wavelengths. The green spectra (blue for 3-exponential fits) are attributable to the lowest triplet 3 do*po. Data for Ir(dimen) at 585 nm (left-bottom) were taken from earlier work 16 and re-analyzed consistently. Lorentzian shape-fits and spectral parameters are displayed in Figures S19-S23 (Ir) and S25, S26, S28, and S29 (Rh).

Ir(dimen). 1 d $\sigma^{*} \rightarrow p\sigma$ excitation (585 nm) of the short/twisted conformer triggers 5-ps relaxation 16 involving 0.41 Å Ir–Ir contraction (DFT estimated). The long/eclipsed conformer excited at 470 nm 16 (reproduced herein exciting at 480 nm) experienced biphasic 0.35- and 4.9-

ps relaxation involving 1.38 Å Ir–Ir contraction and ~42° mutual rotation of the two Ir(C \equiv N-)₄ planes. Independent of excitation wavelength, these relaxation processes produced a 1 do*po TRIR spectrum that converted (~70 ps lifetime) to that of 3 do*po where ESA was 6-7 cm $^{-1}$ higher. Remarkably, coherent oscillations of the ESA bandwidth were observed in the first 2 ps after either excitation. The ~80 cm $^{-1}$ frequency of these oscillations accords with the excited-state Ir–Ir stretch, 7 indicating that fast ν (C \equiv N) vibrations depend on the position of a "slow" ν (Ir–Ir) wavepacket. 16

Analysis of EA_i spectra (Figures 6, S19-S21) revealed differences in the FC 1 d σ^* p σ states of the two conformers that exhibited ESA at 2130.6 cm⁻¹ (585 nm pump, short/eclipsed) and 2137.5 cm⁻¹ (480 nm pump, long/twisted). Relaxation dynamics after 585-nm excitation feature a small ESA 5.4-ps upshift (+1.7 cm⁻¹) and broadening (+3.1 cm⁻¹), whereas more extensive restructuring and desolvation / MeCN re-coordinantion¹⁴ (480 nm pump) are accompanied by an atypical ESA downshift (-2.1 and -1.8 cm⁻¹ in 0.35- and 4.9-ps steps). Relaxation processes after either excitation converged at the ¹dσ*pσ ESA (~2133 cm⁻¹) that evolved with a ~70 ps lifetime to the final 3 d σ^{*} p σ ESA (2140 cm $^{-1}$). (Raw-TRIR analysis gave similar behavior, see Figure S24.) No evidence of GS recovery was observed after 585 nm excitation, where small bleach changes are affected by an overlapping "hidden ESA" (Figure S19). This feature is attributable to the bB₁(A₂) mode whose frequency in this range and intensity gain upon excitation were predicted by DFT (Table S5). Its presence was indicated by deviations of fitted Lorentzians from experimental spectra (Figures S19-S21); and it was fitted as a separate peak in the 480-nmexcited spectra (Figure S21). The bleach area decreases by 16 and 36% in the course of 0.35- and 4.9-ps relaxation, respectively (Figure S21: these numbers should be regarded as upper limits of GS recovery because of bleach overlap with the hidden ESA). There was no evidence for GS recovery accompanying 72-ps ISC (Figures S20-S21).

The initial ESA produced by UV excitation is broader and at lower wavenumbers than that formed by 480 or 585 nm excitation (Figures S22, S23). Fitting of EA_1 gave ESA at 2130.2 cm⁻¹ (375 nm pump) and 2127.2 cm⁻¹ (316 nm pump) with widths of 53 and 57 cm⁻¹, respectively. Time evolution started with two relaxation steps (0.8, ~2 ps at each UV excitation wavelength) that involved small upshifts and large narrowings, presumably converting the FC 1,3 d π p σ states to intermediate states and dissipating excess energy. (The two lifetimes also could reflect parallel evolution of the two excited conformations.) Ultimately, UV-excited Ir(dimen) relaxes to the lowest ³dσ*pσ state whose formation is faster than upon visible excitation and accelerates on going from 375 (43 ps) to 316 nm excitation (21.1 ps). The absence of ~70 ps ISC suggest that the decay of the UV-excited singlet and triplet $d\pi p\sigma$ states to $^3d\sigma^*p\sigma$ bypasses $^1d\sigma^*p\sigma$, while different kinetics indicate decay proceeding through different intermediate states. The bleach area decreased by 16-19% in the course of the second (~2 ps) relaxation step. At 316 nm excitation, the bleach decay continued by a 10% drop in the third step, parallel to 3 do*po population. However, these changes cannot be attributed solely to GS recovery because of overlap with changing "hidden ESA".

Rh(dimen). Irradiation at 480 nm excited the ${}^{1}\text{d}\sigma^{*} \rightarrow p\sigma$ transition of short/twisted conformer(s) and triggered 3-step relaxation/decay (2.4, 36.1, 500 ps) that ultimately recovered the GS (Figures 4, 6, S8). The initial EA_{1} spectrum has a broad ESA feature at 2130.5 cm⁻¹ that is composed of two peaks, plus a bleach that deviates from the fitted curve owing to the presence of overlapping "hidden ESA" estimated at about 2169 cm⁻¹ (Figure S25). The first kinetics step

(2.4 ps) is characterized by a small upshift and narrowing of the main ESA feature, upshift of the experimental points in the negative region closer to the GS bleach position, and a small decay of the bleach area (Figure S25, apparent also in the TRIR 2D map, Figure 4 bottom-left). In analogy to the 5.4-ps relaxation of Ir(dimen) following 585 nm excitation, ¹⁶ the Rh(dimen) 2.4 ps step involves vibrational relaxation and Rh–Rh bond-shortening (0.52 Å, DFT) in the 1 do*po FC state. In the EA_2 spectrum, the 1 do*po relaxed state exhibits an ESA maximum at 2133.6 cm $^{-1}$ (Figure S25). The following 36.1-ps step corresponds to 1 do*po \rightarrow 3 do*po ISC, manifested by a 2 2 cm $^{-1}$ upshift and 2 6 cm $^{-1}$ 1 narrowing, as well as diminishing intensity of both ESA and bleach (by 46–51%) mainly caused by 1 do*po decay to GS. In the last step, both the 3 do*po ESA and the bleach decay, regenerating the ground state with a 500 ps lifetime that matches the previously reported phosphorescence lifetime (<1 ns, 500 ps extrapolated from temperature-dependent decay).

Exciting the long/eclipsed Rh(dimen) conformer at 423 nm generated a very broad TRIR signal whose time evolution required a 5-exponential global fit (Figures 6, S26). The initial signal peaks higher (2143.1 cm⁻¹) than after 480 nm excitation and is much broader (54 vs. 30 cm⁻¹). The first step (0.09 ps, i.e. within the $^{\circ}$ 0.15 ps instrument time resolution) appears as a relaxation/structural change with a $^{\circ}$ 3.7 cm⁻¹ ESA downshift and 4 cm⁻¹ narrowing. These trends continue in the second ultrafast (0.46 ps) step that also includes emergence of a second distinct ESA band in the *EA*₃ spectrum at 2160.3 cm⁻¹ (18.1 cm⁻¹ width). Its formation is clearly apparent also in TRIR 2D maps as well as in raw spectra (Figures 4, S8). It is likely that both bands overlap at shorter time delays within the broad ESA, while the higher lying band upshifts in the course of the 0.46-ps step, becoming a distinct spectral feature in *EA*₃. This "moving ESA" signal vanishes in the third (1.71 ps) relaxation step. However, the TRIR 2D map (Figure 4) shows that

disappearance of the ~2160 cm⁻¹ band coincides with diminished bleach intensity between 3 and 10 ps, suggesting that the extra ESA feature keeps moving to higher wavenumbers into the bleach region. This conclusion was supported by detailed analysis of the EA4 spectrum that suggested the presence of a narrower "extra" ESA in the bleach region (Figure S26). The "moving ESA" was specific for the long/eclipsed Rh(dimen) conformation whose FC ¹dσ*pσ is highly distorted; the relaxed ¹dσ*pσ state is expected to have a Rh–Rh distance ~1.4 Å shorter and a twist angle 42.4° larger than in the GS (based on DFT calculation for the triplet). It is possible that such extensive structural changes proceed through several stages on the ¹dσ*pσ surface and the "moving ESA" evolves from a highly distorted 1 d σ^{*} p σ intermediate structure. EA₄(423 nm), which is attributable to the 1 d σ^{*} p σ_{L} state of the long/eclipsed Rh(dimen) conformer, is different from the 1 d σ^{*} p σ spectrum of the short/twisted conformer [$EA_2(480 \text{ nm})$], suggesting the presence of at least two local minima on the Rh(dimen) ¹dσ*pσ potential energy surface. (The ¹dσ*pσ_L ESA is ~4 cm⁻¹ higher, indicating weaker π -backbonding to $\pi^*(C\equiv N)$, as expected for a longer Rh–Rh distance.) The conclusion that "long" and "short" conformers populate ¹dσ*pσ accords with the anomalous fluorescence excitation spectrum⁶ that is skewed on the high-energy side relative to the visible absorption spectrum, missing the 423-nm feature of the long/eclipsed conformer.

Interestingly, raw Rh(dimen) TRIR spectra obtained in the first picosecond after 423-nm excitation exhibit 1-2 coherent oscillations that are most apparent on the low-wavenumber side of the ESA band (Figure S27). This behavior is similar to Ir(dimen) that, however, exhibits coherent oscillations after excitation at 480 as well as 585 nm.¹⁶

The Rh(dimen) 1 d σ^{*} p σ_{L} ESA shifts down by 1 cm $^{-1}$ and both the bleach and ESA areas decreased by ${}^{\sim}$ 67% with a 19.6 ps lifetime. The product ESA (EA_{5}) matches that of 3 d σ^{*} p σ

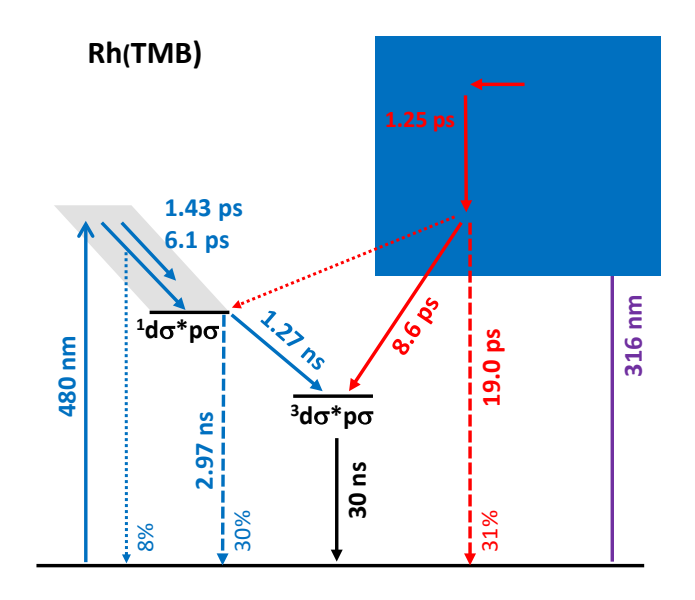
produced after 480-nm excitation (compare Figures S25 bottom-left and Figure S26 bottom). Both the ESA and the bleach decay with a 500-ps lifetime, confirming the last ESA assignment to 3 dσ*pσ. Analysis of raw TRIR spectra (Figure S30) qualitatively accord with the above conclusions from global fitting, except for the additional ~150 ps kinetics of the 3 dσ*pσ ESA wavenumber shift observed upon 480- and 423-nm excitations. Also, the peak wavenumber evolves toward a limiting value ca. 2 cm⁻¹ higher than that of the final ESA. Apparently, 3 dσ*pσ undergoes relatively slow (~150 fs) relaxation during decay to GS (Figure S30).

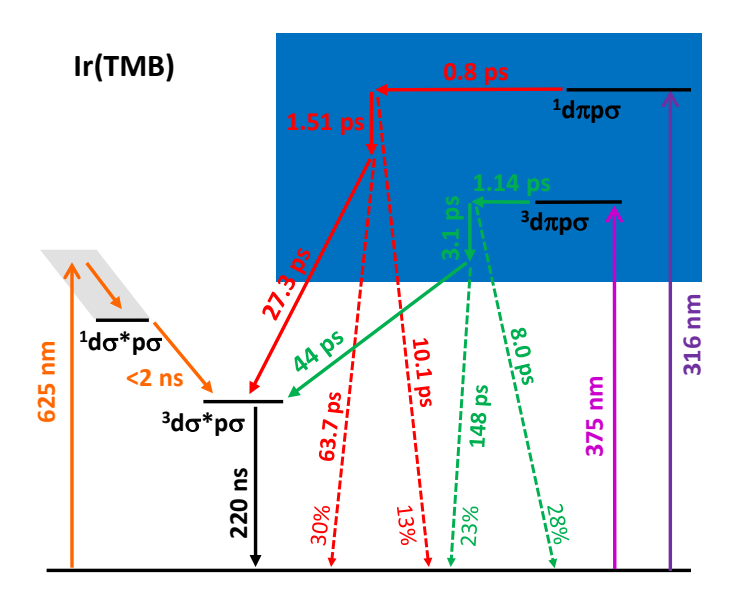
Fitting the spectral evolution after 316-nm excitation (${}^{1}d\pi \rightarrow p\sigma$) of both long/eclipsed and short/twisted Rh(dimen) conformers required 5-exponential kinetics (Figures 6, S28, S29). As the initial spectrum (EA_1) is very broad, a good fit required two Lorentzian functions peaking at 2133 and 2143.2 cm⁻¹ (compare Figures S28 and S29). The two subpicosecond relaxation processes involve very substantial narrowing of the lower band (mostly in the 0.22 ps step) and a large upshift of the higher peak (mainly in the 0.94 ps step; +10.6 cm⁻¹) (Figure S29). The large upshift likely indicates conversion to electronic states with diminished π backbonding. A distinct shoulder emerged at 2157 cm⁻¹ in the EA₃ spectrum during the second relaxation step (0.94 ps). Clearly visible in the 2D map (Figure 4) around 10 ps, it is the equivalent of the 423-nm "moving ESA", attributable to the electronically excited long/eclipsed conformer. The EA4 spectrum that emerged after the following kinetics step (5.13 ps) exhibits the "moving ESA" as a distinct spectral feature (fitted maximum at 2162.5 cm⁻¹), plus a band at 2136.9 cm⁻¹ very near the ³dσ*pσ IR feature observed upon 423- and 480-nm excitation. The "moving ESA" vanishes during the following 12.9 ps step (leading to EA_5) and the bleach area decreases by $\leq 85\%$, while both the peak wavenumber (2137.7 cm⁻¹) and area of the remaining ESA feature stay nearly constant. The

ESA and the negative peak both decay with a $^{\circ}630$ -ps lifetime, supporting the $^{3}d\sigma^{*}p\sigma$ assignment. This behavior suggests that the 5.13-ps step involves two processes: (i) conversion of the UV-excited short/twisted conformer to the lowest $^{3}d\sigma^{*}p\sigma$ state bypassing $^{1}d\sigma^{*}p\sigma$; and (ii) trapping the excited long/eclipsed conformer in a highly distorted intermediate state from which it decays directly to the ground state.

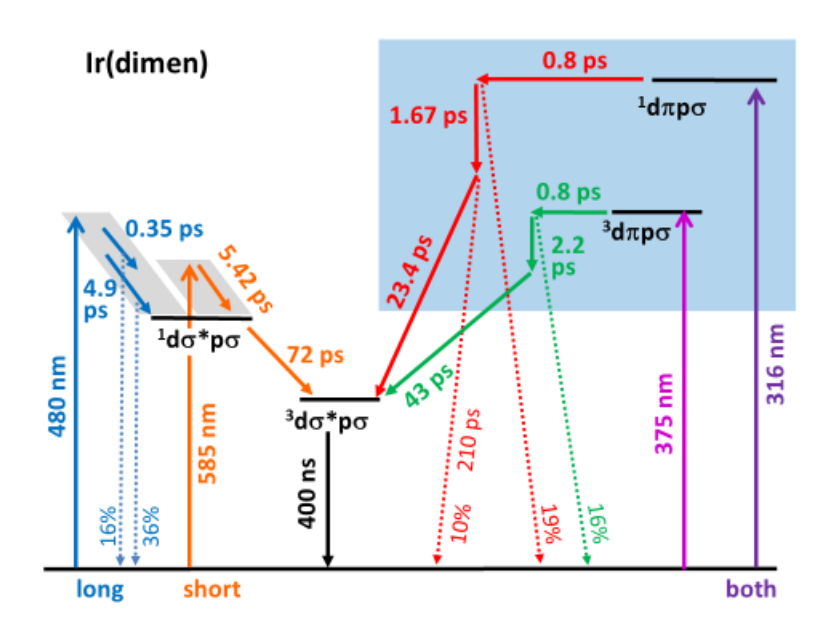
Finally, it should be noted that the ${}^3\text{d}\sigma^*p\sigma$ ESA obtained upon 316-nm excitation peaks ${}^{\sim}2$ cm $^{-1}$ higher than that measured at 480 or 423 nm excitation; and a similar difference was observed when fitted with two ESA Lorentzians. In this case, the ${}^3\text{d}\sigma^*p\sigma$ ESA from global and raw-TRIR analyses matched each other and the ${}^{\sim}150$ -ps triplet relaxation was not observed.

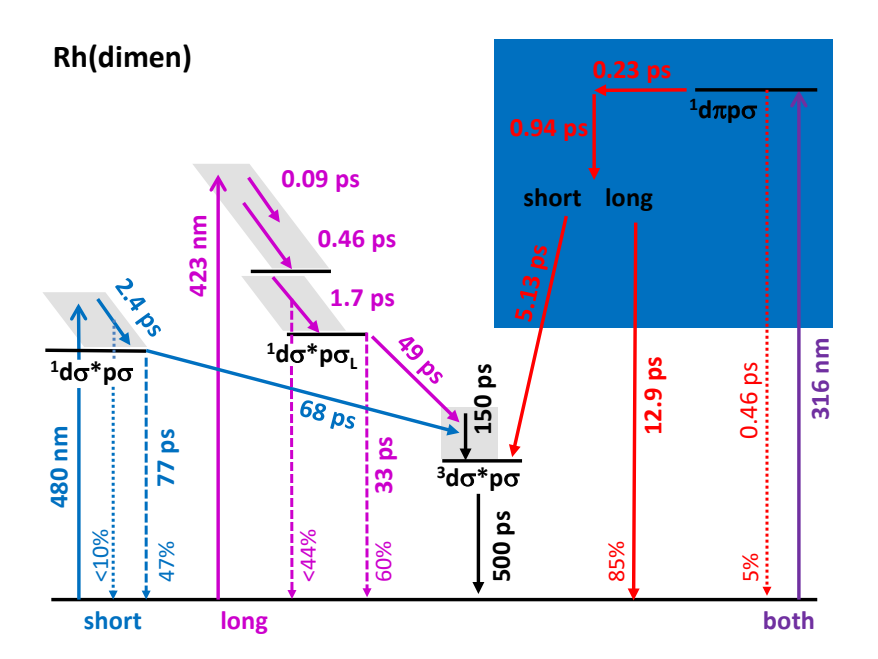
Solvent IR transients. Most of the TRIR spectra (Figures S5-S8) exhibit weak positive signals at 2250 cm $^{-1}$ and (much weaker) 2290 cm $^{-1}$, at the positions of the v(NC) peaks of the MeCN solvent (split by Fermi resonance). These signals emerge shortly after excitations. They were observed at all excitation wavelengths but were most prominent at 316 nm and more intense for Ir than Rh complexes (Figure S32). Their presence could indicate vibrational energy transfer to the solvent and/or solvent restructuring after excitation, in accord with X-ray scattering experiments on Ir(dimen). 14





Scheme 2. Excited-state dynamics of Rh(TMB) and Ir(TMB) upon visible or UV excitation. Horizontal bars represent relaxed electronic states, gray areas their higher vibrational levels. The light-blue rectangles stand for manifolds of high-lying electronic excited states. Numbers parallel to arrows were estimated from measured lifetimes (Table 1) and GS recovery yields and represent time constants of the corresponding steps. Measured lifetimes are placed horizontally. Data from this work, Rh(TMB) 3 d * p σ lifetime from ref. 32 ; Ir(TMB) 1,3 d * p σ lifetimes from ref. 38





Scheme 3. Excited-state dynamics of Ir(dimen) and Rh(dimen) upon visible or UV excitation. Horizontal bars represent relaxed electronic states, gray areas their higher vibrational levels. The light-blue rectangles stand for manifolds of high-lying electronic excited states. Numbers parallel to arrows were estimated from measured lifetimes (Table 1) and GS recovery yields and represent time constants of the corresponding steps. Measured lifetimes are placed horizontally.

Excited-state dynamics. Excited-state deactivation mechanisms of the investigated di-isocyanide complexes are summarized in Schemes 2 and 3. The photophysics was inferred from changes of

 $v(C\equiv N)$ IR-active modes upon excitation, supported and guided by DFT and perturbational spinorbit TDDFT calculations. Proposed kinetics and mechanisms are compatible with photoluminescence lifetimes and yields, 6 , 32 optical time-resolved spectra, 7 as well as with information from time-resolved X-ray techniques 13 , 14 and QM/MM simulations. 14 , 21 The sensitivity of IR-active $v(C\equiv N)$ modes to the nature of the excited state comes from strong $\pi^*(C\equiv N)$ participation in the p σ orbital and predominant M–M localization of the other spectroscopically/photophysically important orbitals, $d\pi$ and $d\sigma^*$. Each of the $^{1,3}d\sigma^*p\sigma$ states has a large MMLCT component and the increased $\pi^*(C\equiv N)$ population shifts $v(C\equiv N)$ vibrations to lower energies. An even larger downshift occurs upon $d\pi \rightarrow p\sigma$ excitation, owing to the participation of occupied $\pi(C\equiv N)$ orbitals in $d\pi$, which in turn imparts ligand-centered $\pi\pi^*$ character to $d\pi p\sigma$ states, thereby distinguishing them from $d\sigma^*p\sigma$ states by TRIR. These shifts accord with calculated C $\equiv N$ bond orders that decrease according to: GS > $^1d\pi p\sigma$ > $^1d\sigma^*p\sigma$ (Table S28 in the SI, section 11).

Binuclear metal-di-isocyanide photophysics can be summarized as follows: (i) the lowest ${}^1\text{d}\sigma^*p\sigma$ excited state undergoes ISC to the lowest ${}^3\text{d}\sigma^*p\sigma$ state with a rate determined by SOC as well as by structural flexibility (compare TMB and dimen complexes); (ii) visible-light-populated FC ${}^1\text{d}\sigma^*p\sigma$ states and their initial relaxation mechanisms are structure-dependent (cf. differences between long/eclipsed and short/twisted M(dimen) conformations); (iii) UV-excited ${}^1\text{d}\pi p\sigma$ and (for Ir) ${}^3\text{d}\pi p\sigma$ states decay along excitation-specific pathways that converge only at the level of the lowest triplet, ${}^3\text{d}\sigma^*p\sigma$. Decay pathways of both UV-excited d $\pi p\sigma$ states largely bypass the lowest excited singlet, ${}^1\text{d}\sigma^*p\sigma$; (iv) the rate of ${}^3\text{d}\sigma^*p\sigma$ population increases on going from visible to 375 nm, and to 316 nm excitation; and (v) GS recovery accompanies most excited-state-

conversion and ISC steps, as well as some structure-relaxing processes, decreasing ${}^3\text{d}\sigma^*p\sigma$ formation quantum yields, which unfortunately diminish photocatalyst efficiencies. Direct decay from upper states to GS is most pronounced in the case of structurally flexible Rh(dimen), reducing the phosphorescence quantum yield of the long/eclipsed conformer. 6,36,39

The highest-energy excitation at 316 nm populates an FC state that is 95-97% (Rh) and 54-76% (Ir) 1 dπpσ, while 3 dπpσ and (less) 3 dδ,δ*pσ contributions make up the rest. M–M bond orders were calculated 2.2 – 2.8 times smaller than in $^{1}\text{d}\sigma^*\text{p}\sigma$ (Table S28, Figure S35), suggesting smaller M–M contraction after UV excitation, in accord with the narrow 316-nm absorption band (Figure 2). The 316 nm excited 1 d π p σ state falls within a manifold of electronic excited states (light-blue blocks in Schemes 2, 3) that provide ISC pathways that ultimately lead to ³dσ*pσ, bypassing the lowest singlet state. The subpicosecond departure time from the FC state is shorter than the 5-30 ps arrival time to 3 do * po, with one or two distinguishable kinetics steps. Although it is not possible to pinpoint the intermediate states, it is worth noting that many close-lying lower states have substantial 3 d σ p σ /d σ *p σ * character (cyan in SI SOC tables). These states could be populated by symmetry-allowed ISC from 1 d π p σ and their structural difference along the M– M coordinate would increase vibrational overlap with the 3 d σ^{*} p σ lowest triplet. The 5-30 ps 3 do*po arrival time increases in the order Rh(dimen) < Rh(TMB) < Ir(TMB) \cong Ir(dimen). Decay of the 1 d π p σ -excited long/eclipsed Rh(dimen) conformation bypasses the 3 d σ *p σ lowest triplet, decaying to GS with a ~13 ps time constant, possibly by crossing the GS potential energy surface of the short/twisted conformer.

Irradiation of the Ir complexes at 375 nm populates a predominantly $^3d\pi p\sigma$ state (85%) with 10% $^1d\pi p\sigma$ admixture. As in the case of 316 nm excited $^1d\pi p\sigma$, $^3d\pi p\sigma$ decays to $^3d\sigma^*p\sigma$. The

lowest ${}^1\text{d}\sigma^*p\sigma$ singlet is bypassed even if ${}^3\text{d}\pi p\sigma \rightarrow {}^1\text{d}\sigma^*p\sigma$ ISC is symmetry allowed. Whereas the departure times after 316 and 375 nm excitations are comparable, the ${}^3\text{d}\sigma^*p\sigma$ arrival time upon 375 nm excitation is distinctly slower, ca. 40 ps; and intermediate lifetimes are slower as well. Different kinetics following 316 and 375 nm excitations indicate separate deactivation pathways. In particular, these kinetics show that ${}^3\text{d}\pi p\sigma$ is not involved in the ${}^1\text{d}\pi p\sigma$ decay. The immediate precursor states, from which ${}^3\text{d}\sigma^*p\sigma$ is populated, also are different.

Irradiation with visible light excites the ${}^{1}d\sigma^{*}\rightarrow p\sigma$ transition. The transition energy decreases with M-M bond strengthening, allowing the two M(dimen) conformers to be studied separately. Comparison of the two conformers highlights the importance of structural factors. Excitation of short/twisted Ir(dimen) (585 nm) and Rh(dimen) (480 nm) triggers a relatively simple response whereby relaxed ¹dσ*pσ is formed with 4.9 (Ir) and 2.4 ps (Rh) singleexponential kinetics, characterized by a small ESA upshift. Rh(TMB) (short/twisted structure) behaves similarly and its FC 1 d σ^{*} p σ state relaxes in 1.43 and 6.1 ps steps. In all cases, the M–M distance shortens by 0.3 - 0.5 Å, and the twist angle slightly increases $(0.4 - 4.3^{\circ})$. In Rh(TMB), one or more ligands likely refold to accommodate the shortened M-M unit. The long/eclipsed M(dimen) conformers are trapped in elongated/eclipsed structures by a balance between electronic factors (namely dispersion and $\pi\pi$ interactions) tending toward short M–M distances, and bridging-ligand strain that keeps the metal atoms relatively far apart.³⁹ This situation is preserved in FC ¹dσ*pσ states prepared by 480 (Ir) and 423 nm (Rh) excitation whose IR-intense v(C≡N) modes occur about 7 (Ir) and 12 cm⁻¹ (Rh) higher than after exciting the short/twisted conformers. Relaxation of FC-1dσ*pσ involves coupled ~1.4 Å M–M contraction, ~42° twist, and solvent-shell restructuring 14 accompanied by a $v(C \equiv N)$ downshift, best seen in raw-TRIR fits

(Figures S24, S30). Relaxation is bi- or triexponential with time constants ranging from hundreds of femtoseconds to picoseconds. It is faster for the more flexible Rh(dimen) complex, where ${}^1\text{d}\sigma^*p\sigma_L$ IR spectrum differs from that of ${}^1\text{d}\sigma^*p\sigma$ prepared by 480 nm excitation of the short/twisted conformer. Of interest is that the ${}^1\text{d}\sigma^*p\sigma_L$ state is much less emissive, as demonstrated by a mismatch between fluorescence excitation and absorption spectra above 400 nm.⁶ Apparently, the shallow (rugged) GS potential energy surface is mapped onto the lowest excited singlet and the long/twisted Rh(dimen) conformer becomes trapped in a local ${}^1\text{d}\sigma^*p\sigma_L$ minimum, from which it decays to the triplet before equilibrating with ${}^1\text{d}\sigma^*p\sigma$.

There have been many lively discussions of the factors that control ISC between the singlet and triplet dσ*pσ states of d⁸d⁸ di-isocyanides and Pt(pop).¹ Although ISC is a symmetryforbidden process, its rate varies from 0.7 ps to ~2 ns, depending on metal, ligands, structural rigidity, solvent, as well as temperature. Several models have been proposed, assuming thermal population of an intermediate triplet state^{45, 46} whose energy might be temporarily lowered by solvent fluctuations and asymmetric solvation, ¹⁸ or a thermally-induced molecular distortion that would lift symmetry restrictions and/or enhance second-order SOC between the dσ*pσ singlet and triplet through a higher-lying 3 d π p σ state. 3 , 47 Our pSOC-TDDFT calculations revealed a small SOC-induced 3 d π p σ admixture into both singlet and triplet d σ *p σ states (marked green in S9, S12, S15, S18, S21, and S24). The slow ISC rate (1.27 ns) observed for Rh(TMB) is attributable to weak SOC and a very small 3 d π p σ triplet contribution to 1 d σ *p σ (Table S12, Figure S33). However, the 3 d π p σ admixture is equally small in Rh(dimen) (Tables S24, S21) but ISC is more than 10 times faster! Moreover, the ISC rates are comparable in Rh(dimen) and Ir(dimen), despite larger SOC in the latter. These observations point to the importance of structural flexibility, since Rh(dimen) is the most flexible of the four investigated complexes.^{6, 36, 39} Accordingly, restricting the structural flexibility by going from a MeCN solution to a PMMA film extends the Rh(dimen) 1 do*po lifetime from 36 (TRIR) to 230 ps (fluorescence decay).⁶ The notion that ISC in d⁸d⁸ complexes is facilitated by molecular distortions also is supported by the much shorter 1 do*po lifetime in Pt(pop) (0.7 ps in MeCN at RT)¹⁸ than in rigid Pt(pop-BF₂) (1.6 ns),⁸ despite very similar electronic structures.³ A mechanism involving thermal population of an intermediate state seems less likely because of the energetic isolation of the 1 do*po state. Energy gaps to upper states (>5500 cm⁻¹ at optimized geometries, Figure S34 and pSOC-TDDFT SI tables) are higher than experimental ISC-activation energies.¹

■ CONCLUDING REMARKS

In terms of photophysics, d⁸d⁸ complexes are in a class of their own. Nevertheless, comparison with mononuclear complexes provides interesting insights into some of the fundamental questions, ^{48, 49} among them how energy dissipation after optical excitation depends on the nature of the optically accessed state, density of states, and vibrational dynamics.

The most striking difference can be seen in the rate and nature of energy dissipation from high-lying states, which is femtosecond and virtually continuous in $Ir(ppy)_3^{33}$ (ppy = 2-phenyl-pyridine), as well as in Ru(II) and Fe(II) polypyridyl complexes,^{49, 50} in contrast with picosecond cascades of kinetically and spectroscopically distinct steps in d^8d^8 isocyanides. For example, UV-excited ligand-centered states of $Ir(ppy)_3$ decay with a 70 fs lifetime to the lowest 3 MLCT state formed with the same lifetime, indicating that all intermediate steps are much faster, ≤ 10 fs. 33 About 1.6 eV is dissipated in a series of conical intersections (CI), vibrational energy is transferred

to low-frequency modes in less than a single vibrational period, intramolecular vibrational redistribution (IVR), internal conversion, and ISC are entangled and cannot be distinguished experimentally or conceptually. Similarly, observation of fluorescence that mirrors the ¹MLCT absorption band of $[M(bpy)_3]^{2+}$ (M = Fe, Ru) 30 fs after excitation at higher energies is consistent with convoluted femtosecond relaxation.^{49, 50} This behavior likely is enabled by a high density of states that span the whole energy range from the FC state to ³MLCT. Structural differences between excited states involve many coordinates along which CIs may arise. In contrast, the 0.2-1.3 ps departure times from high-lying $d\pi p\sigma^*$ states in d^8d^8 di-isocyanides are faster than the 20-40 ps arrival times to the lowest ³dσpσ* state, and relaxation proceeds through several progressively slower picosecond steps. Unlike d⁶ mononuclear complexes, d⁸d⁸ di-isocyanides have a single dominant coordinate, M-M. Individual electronic states differ in M-M distances and symmetries with respect to the M-M unit, namely the C4 and perpendicular C2 rotations of the $M_2(C=N-)_8$ core that impose rather strict selection rules. The density of states is lower, consisting of closely spaced sets separated by energy gaps (Figure S34). Bypassing the lowest singlet, $d\pi p\sigma^*$ relaxation has to overcome a 1.1-1.5 eV gap that separates $^3d\sigma^*p\sigma$ from the manifold of higher states, likely enabled by large structural differences and, hence, surface crossings along the M-M coordinate. It is important to note that this process is fastest for structurally flexible Rh(dimen), where large-amplitude fluctuations explore configurational space and facilitate arrival into the surface-crossing regions. Importantly, the lower density of states, energy gaps, and symmetry restrictions on IC and ISC processes, as well as on promoting vibrations, appear to be the main factors limiting rates of stepwise energy dissipation from highlying states. It is of interest that the same factors are responsible for the UV absorption spectral

pattern of d⁸d⁸ di-isocyanides: one or two sharp intense bands separated by several very weak absorption features (Figure 2), in contrast to broad overlapping bands over most of the UV region in the case of d⁶ complexes.

Within the d^8d^8 family, relaxation of high-lying states also was investigated for Pt(pop) and Pt(pop-BF₂).¹⁹ UV-excited spin-mixed LMMCT (ligand to metal-metal charge transfer) states³ were found to convert to the lowest ${}^3d\sigma^*p\sigma$ triplet without discernible intermediate steps, and with a 0.25-0.3 ps time constant preserving vibrational coherence along the Pt–Pt coordinate. The ${}^1d\sigma^*p\sigma$ state is largely bypassed as in the di-isocyanide complexes.

Concerning the low-lying states, ISC from optically excited ¹MLCT states to the lowest MLCT triplet in mononuclear polypyridyl complexes occurs in about 30 fs for Fe^{II} and Ru^{II}, and ≤100 for Os^{II}. ⁴⁹⁻⁵³ In the case of Re^I(L)(CO)₃(polypyridyl) complexes, ¹MLCT fluorescence decays in 80-150 and 300-1200 fs steps (depending on complex and solvent), ⁵⁴⁻⁵⁶ interpreted by nonadiabatic dynamics calculations⁵⁷ as units-of-femtoseconds electronic evolution completed during hundreds-of-femtoseconds IVR. All these ISC processes are much faster than in d⁸d⁸ diisocyanides (50 ps − 1.3 ns), Pt(pop) (700 fs − 30 ps, depending on solvent) and rigid Pt(pop-BF₂) (2.1 ns), ^{1, 8, 17, 18} as well as in [Pt(ppy)(μ-L)]₂ complexes (L = pyrazolates, 2-hydroxopyridines) where the ISC time constant (0.3-1 ps) depends on L as well as on the detection wavelength. ^{5, 58} In all these complexes, dσ*pσ singlet–triplet ISC is symmetry forbidden, which can be overcome by structural fluctuations or, as was shown ^{5, 58} for [Pt(ppy)(μ-L)]₂, by surface crossing with an intermediate triplet state of different orbital origin. Common to all these classes of metal complexes is a lack of correlation between ISC rates and spin-orbit coupling strength of the metal (or the donor ⁵⁴⁻⁵⁶) atom, whereas structural dynamics and flexibility are closely related.

ASSOCIATED CONTENT

The Supporting Information is available free of charge at

Calculated molecular structures, harmonic v(C=N) vibrations, spin-orbit and spin-free electronic transitions, and molecular orbitals. Raw TRIR spectral, shape analysis of evolution-associated and raw spectra. Experimental and computational details.

AUTHOR INFORMATION

Corresponding Authors

Harry B. Gray – Beckman Institute, California Institute of Technology, Pasadena, California 91125, United States; orcid.org/0000-0002-7937-7876; Email: hbgray@caltech.edu

Stanislav Záliš – J. Heyrovský Institute of Physical Chemistry, Academy of Sciences of the Czech Republic, CZ-18223 Prague, Czech Republic; orcid.org/0000-0003-4345-3205; Email: zalis@jhinst.cas.cz

Antonín Vlček – Department of Chemistry, Queen Mary University of London, E1 4NS London, United Kingdom; J. Heyrovský Institute of Physical Chemistry, Academy of Sciences of the Czech Republic, CZ-18223 Prague, Czech Republic; orcid.org/0000-0002-6413-8311; Email: a.vlcek@qmul.ac.uk

Authors

Martin Pižl – J. Heyrovský Institute of Physical Chemistry, Academy of Sciences of the Czech Republic, Dolejškova 3, CZ-182 23 Prague, Czech Republic; Department of Inorganic Chemistry, University of Chemistry and Technology, Prague, Technická 5, CZ-166 28 Prague, Czech Republic; orcid.org/0000-0003-4990-9218

Bryan M. Hunter – Rowland Institute at Harvard, Cambridge, Massachusetts, 02142, United States; orcid.org/0000-0001-8559-9304

Igor V. Sazanovich – Central Laser Facility, Research Complex at Harwell, STFC, Rutherford Appleton Laboratory, Harwell Oxford, Didcot, Oxfordshire, OX11 OQX, United Kingdom; orcid.org/0000-0002-8000-7645.

Michael Towrie – Central Laser Facility, Research Complex at Harwell, STFC, Rutherford Appleton Laboratory, Harwell Oxford, Didcot, Oxfordshire, OX11 OQX, United Kingdom; orcid.org/0000-0002-1305-701X

Complete contact information is available at:

Notes

The authors declare no competing financial interest.

ACKNOWLEDGMENTS

This research was supported by the Czech Science Foundation (GAČR) Grant No. 21-05180S, the Czech Ministry of Education (MŠMT) Grant No. LTAUSA18026, EPSRC (UK) Grant No.

EP/R029687/1, the STFC Rutherford Appleton Laboratory (UK), the United States National Science Foundation (CHE-1763429), and the Arnold and Mabel Beckman Foundation.

REFERENCES

- 1. Gray, H. B.; Záliš, S.; Vlček, A., Electronic structures and photophysics of d⁸-d⁸ complexes *Coord. Chem. Rev.* **2017**, *345*, 297-317.
- 2. Mann, K. R.; Gordon II, J. C.; Gray, H. B., Characterization of Oligomers of Tetrakis(phenyl isocyanide)rhodium(I) in Acetonitrile Solution. *J. Am. Chem. Soc.* **1975**, *97*, 3553-3555.
- 3. Záliš, S.; Lam, Y. C.; Gray, H. B.; Vlček, A., Jr., Spin–Orbit TDDFT Electronic Structure of Diplatinum(II,II) Complexes. *Inorg. Chem.* **2015**, *54*, 3491–3500.
- 4. Brown-Xu, S. E.; Kelley, M. S. J.; Fransted, K. A.; Chakraborty, A.; Schatz, G. C.; Castellano, F. N.; Chen, L. X., Tunable Excited-State Properties and Dynamics as a Function of Pt–Pt Distance in Pyrazolate-Bridged Pt(II) Dimers. *J. Phys. Chem. A* **2016**, *120*, 543–550.
- 5. Kim, P.; Valentine, A. J. S.; Roy, S.; Mills, A. W.; Chakraborty, A.; Castellano, F. N.; Li, X.; Chen, L. X., Ultrafast Excited-State Dynamics of Photoluminescent Pt(II) Dimers Probed by a Coherent Vibrational Wavepacket. *J. Phys. Chem. Lett.* **2021**, *12*, 6794–6803.
- 6. Miskowski, V. M.; Rice, S. F.; Gray, H. B.; Dallinger, R. F.; Milder, S. J.; Hill, M. G.; Exstrom, C. L.; Mann, K. R., Spectroscopy and Photophysics of Rh₂(dimen)₄²⁺ (dimen = 1,8-Diisocyanomenthane). Exceptional Metal-Metal Bond Shortening in the Lowest Electronic Excited States. *Inorg. Chem.* **1994**, *33*, 2799-2807.
- 7. Hartsock, R. W.; Zhang, W.; Hill, M. G.; Sabat, B.; Gaffney, K. J., Characterizing the Deformational Isomers of Bimetallic $Ir_2(dimen)_4^{2+}$ (dimen = 1,8-diisocyano-p-menthane) with Vibrational Wavepacket Dynamics. *J. Phys. Chem. A* **2011**, *115*, 2920–2926.
- 8. Durrell, A. C.; Keller, G. E.; Lam, Y.-C.; Sýkora, J.; Vlček, A., Jr.; Gray, H. B., Structural Control of ¹A_{2u}-to-³A_{2u} Intersystem Crossing in Diplatinum(II,II) Complexes. *J. Am. Chem. Soc.* **2012**, *134*, 14201–14207.
- 9. van der Veen, R. M.; Milne, C. J.; El Nahhas, A.; Lima, F. A.; Pham, V.-T.; Best, J.; Weinstein, J. A.; Borca, C. N.; Abela, R.; Bressler, C.; Chergui, M., Structural Determination of a Photochemically Active Diplatinum Molecule by Time-Resolved EXAFS Spectroscopy. *Angew. Chem. Int. Ed.* **2009**, *48*, 2711 –2714.
- 10. Yasuda, N.; Uekusa, H.; Ohashi, Y., X-ray Analysis of Excited-State Structures of the Diplatinum Complex Anions in Five Crystals with Different Cations. *Bull. Chem. Soc. Jpn.* **2004,** *77*, 933–944.
- 11. Kim, C. D.; Pillet, S.; Wu, G.; Fullagar, W. K.; Coppens, P., Excited-state structure by time-resolved X-ray diffraction. *Acta Crystallogr. A* **2002**, *58*, 133-137.
- 12. Christensen, M.; Haldrup, K.; Bechgaard, K.; Feidenhans'l, R.; Kong, Q.; Cammarata, M.; Lo Russo, M.; Wulff, M.; Harrit, N.; M.M., N., Time-Resolved X-ray Scattering of an Electronically Excited State in Solution. Structure of the ${}^3A_{2u}$ State of Tetrakis- μ -pyrophosphitodiplatinate(II). *J. Am. Chem. Soc.* **2009**, *131*, 502–508.
- 13. Haldrup, K.; Harlang, T.; Christensen, M.; Dohn, A.; van Driel, T. B.; Kjær, K. S.; Harrit, N.; Vibenholt, J.; Guerin, L.; Wulff, M.; Nielsen, M. M., Bond Shortening (1.4 A) in the Singlet and Triplet Excited States of [Ir₂(dimen)₄]²⁺ in Solution Determined by Time-Resolved X-ray Scattering. *Inorg. Chem.* **2011**, *50*, 9329–9336.

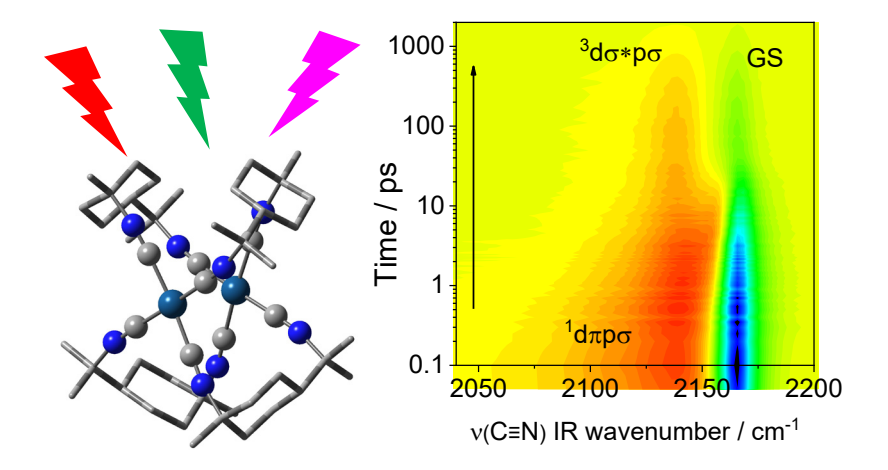
- 14. van Driel, T. B.; Kjær, K. S.; Hartsock, R. W.; Dohn, A. O.; Harlang, T.; Chollet, M.; Christensen, M.; Gawelda, W.; Henriksen, N. E.; Kim, J. G.; Haldrup, K.; Kim, K. H.; Ihee, H.; Kim, J.; Lemke, H.; Sun, Z.; Sundström, V.; Zhang, W.; Zhu, D.; Møller, K. B.; Nielsen, M. M.; Gaffney, K. J., Atomistic characterization of the active-site solvation dynamics of a model photocatalyst. *Nat. Comm.* **2016**, *7*, 13678.
- 15. Doorn, S. K.; Gordon, K. C.; Dyer, R. B.; Woodruff, W. H., Time-Resolved Infrared Spectroscopy of Rh₂(1,3-diisocyanopropane)₄(BPh₄)₂. *Inorg. Chem.* **1992,** *31*, 2284-2285.
- 16. Pižl, M.; Hunter, B. M.; Greetham, G. M.; Towrie, M.; Záliš, S.; Gray, H. B.; Vlček, A., Ultrafast Wiggling and Jiggling: $Ir_2(1,8\text{-diisocyanomenthane})_4^{2+}$. *J. Phys. Chem. A* **2017**, *121*, 9275–9283.
- 17. van der Veen, R. M.; Cannizzo, A.; van Mourik, F.; Vlček, A., Jr.; Chergui, M., Vibrational Relaxation and Intersystem Crossing of Binuclear Metal Complexes in Solution. *J. Am. Chem. Soc.* **2011**, *133*, 305-315.
- 18. Monni, R.; Capano, G.; Auböck, G.; Gray, H. B.; Vlček, A.; Tavernelli, I.; Chergui, M., Vibrational coherence transfer in the ultrafast intersystem crossing of a diplatinum complex in solution. *Proc. Natl. Acad. Sci. U.S.A.* **2018**, *115*, E6396–E6403.
- 19. Monni, R.; Auböck, G.; Kinschel, D.; Aziz-Lange, K. M.; Gray, H. B.; Vlček, A.; Chergui, M., Conservation of vibrational coherence in ultrafast electronic relaxation: The case of diplatinum complexes in solution. *Chem. Phys. Lett.* **2017**, *683*, 112-120.
- 20. Levi, G.; Pápai, M.; Henriksen, N. E.; Dohn, A. O.; Møller, K. B., Solution Structure and Ultrafast Vibrational Relaxation of the PtPOP Complex Revealed by ΔSCF-QM/MM Direct Dynamics Simulations. *J. Phys. Chem. C* **2018**, *122*, 7100–7119.
- 21. Dohn, A. O.; Jónsson, E. O.; Kjær, K. S.; van Driel, T. B.; Nielsen, M. M.; Jacobsen, K. W.; Henriksen, N. E.; Møller, K. B., Direct Dynamics Studies of a Binuclear Metal Complex in Solution: The Interplay Between Vibrational Relaxation, Coherence, and Solvent Effects. *J. Phys. Chem. Lett.* **2014**, *5*, 2414–2418.
- 22. Vlček, A., Jr.; Gray, H. B., Binuclear Platinum(II) Photochemistry. Rates of Hydrogen Atom Transfer from Organometallic Hydrides to Electronically Excited $Pt_2(P_2O_5H_2)_4^{4-}$. J. Am. Chem. Soc. **1987**, 109, 286-287.
- 23. Vlček, A., Jr.; Gray, H. B., Binuclear Platinum(II) Photochemistry. Reactions of Organometallic Hydrides with Electronically Excited Tetrakis(pyrophosphito)diplatinate(II). *Inorg. Chem.* **1987**, *26*, 1997-2001.
- 24. Harvey, E. L.; Stiegman, A. E.; Vlček, A., Jr.; Gray, H. B., Dihydridotetrakis(pyrophosphito(2-))diplatinate(III). *J. Am. Chem. Soc.* **1987**, *109*, 5233-5235.
- 25. Zhong, J.-J.; To, W.-P.; Liu, Y.; Lu, W.; Che, C.-M., Efficient acceptorless photodehydrogenation of alcohols and N-heterocycles with binuclear platinum(II) diphosphite complexes. *Chem. Sci.* **2019**, *10*, 4883–4889.
- 26. Smith, D. C.; Gray, H. B., Atom-Transfer Reactivity of Binuclear d⁸ Complexes. In *ACS Symposium Series 394. The Challenge of d and f Electrons.*, Salahub, D. R.; Zerner, M. C., Eds. American Chemical Society: Washington, DC, 1989; pp 356-365.
- 27. Smith, D. C.; Gray, H. B., Photochemistry of Binuclear d⁸ Complexes. *Coord. Chem. Rev.* **1990,** *100*, 169-181.

- 28. Sweeney, R. J.; Harvey, E. L.; Gray, H. B., Photoreactions of tetrakis(μ -pyrophosphito)diplatinate(II) with alcohols and hydrocarbons. *Coord. Chem. Rev.* **1990**, *105*, 23-34.
- 29. Mann, K. R.; Lewis, N. S.; Miskowski, V. M.; Erwin, D. K.; Hammond, G. S.; Gray, H. B., Solar Energy Storage. Production of Hydrogen by 546-nm Irradiation of a Dinuclear Rhodium(I) Complex in Acidic Aqueous Solution. *J. Am. Chem. Soc.* **1977**, *99*, 5525-5526.
- 30. Sigal, I. S.; Mann, K. R.; Gray, H. B., Solar Energy Storage Reactions. Thermal and Photochemical Redox Reactions of Polynuclear Rhodium Isocyanide Complexes. *J. Am. Chem. Soc.* **1980**, *102*, 7252-7256.
- 31. Smith, D. C.; Miskowski, V. M.; Mason, W. R.; Gray, H. B., Electronic Absorption and MCD Spectra of $M_2(TMB)_4^{2+}$, M = Rh and Ir. A Valence-Bond Description of the Upper Electronic Excited States. *J. Am. Chem. Soc.* **1990**, *112*, 3759-3767.
- 32. Miskowski, V. M.; Rice, S. F.; Gray, H. B., Excited-State Decay Processes of Binuclear Rhodium(I) Isocyanide Complexes. *J. Phys. Chem.* **1993**, *97*, 4277-4283.
- 33. Messina, F.; Pomarico, E.; Silatani, M.; Baranoff, E.; Chergui, M., Ligand-Centred Fluorescence and Electronic Relaxation Cascade at Vibrational Time Scales in Transition-Metal Complexes. *J. Phys. Chem. Lett.* **2015**, *6*, 4475–4480.
- 34. Wang, F.; Ziegler, T., A simplified relativistic time-dependent density-functional theory formalism for the calculations of excitation energies including spin-orbit coupling effect. *J. Chem. Phys.* **2005**, *123*, 154102.
- 35. Wang, F.; Ziegler, T.; van Lenthe, E.; van Gisbergen, S.; Baerends, E. J., The calculation of excitation energies based on the relativistic two-component zeroth-order regular approximation and time-dependent density-functional with full use of symmetry. *J. Chem. Phys.* **2005**, *122*, 204103.
- 36. Exstrom, C. L.; Britton, D.; Mann, K. R.; Hill, M. G.; Miskowski, V. M.; Schaefer, W. P.; Gray, H. B.; Lamanna, W. M., Structures of $[M_2(dimen)_4](Y)_2$ (M = Rh, Ir; dimen = 1,8-Diisocyanomenthane; Y = PF₆, Tetrakis[3,5-bis(trifluoromethyl)phenyl]borate, B(C₆H₅)₄) Crystals Featuring an Exceptionally Wide Range of Metal-Metal Distances and Dihedral Twist Angles. *Inorg. Chem.* **1996**, *35*, 549-550.
- 37. Mann, K. R.; Thich, J. A.; Bell, R. A.; Coyle, C. L.; Gray, H. B., Crystal Structure Analyses of Rh₂(bridge)₄(BPh₄)₂.CH₃CN and Rh₂(TM₄-bridge)₄(PF₆)₂.2CH₃CN. Further Electronic Spectral Studies of Binuclear Rhodium(I) Isocyanide Complexes *Inorg. Chem.* **1980**, *19*, 2462-2468.
- 38. Smith, D. C. Electronic Structure and Photochemical Reactivity of Binuclear Metal Complexes. Ph.D. Dissertation, California Institute of Technology, Pasadena, California, 1989.
- 39. Hunter, B. M.; Villahermosa, R. M.; Exstrom, C. L.; Hill, M. G.; Mann, K. R.; Gray, H. B., M–M Bond-Stretching Energy Landscapes for $M_2(dimen)_4^{2+}$ (M = Rh, Ir; dimen = 1,8-Diisocyanomenthane) Complexes. *Inorg. Chem.* **2012**, *51*, 6898–6905.
- 40. Rice, S. F. Optical Spectroscopy of Square Planar d⁸ Dimers. Ph.D. Dissertation, California Institute of Technology, Pasadena, California, 1982.
- 41. Záliš, S.; Hunter, B. M.; Gray, H. B.; Vlček, A., Electronic Structures of Reduced and Superreduced Ir₂(1,8-diisocyanomenthane)₄ⁿ⁺ Complexes. *Inorg. Chem.* **2017**, *56*, 2874–2883.
- 42. Coppens, P.; Gerlits, O.; Vorontsov, I. I.; Kovalevsky, A. Y.; Chen, Y.-S.; Graber, T.; Gembicky, M.; Novozhilova, I. V., A very large Rh–Rh bond shortening on excitation of the

- $[Rh_2(1,8-diisocyano-p-menthane)_4]^{2+}$ ion by time-resolved synchrotron X-ray diffraction. *Chem. Commun.* **2004**, 2144–2145.
- 43. Rice, S. F.; Gray, H. B., Metal-Metal Interactions in Binuclear Rhodium Isocyanide Complexes. Polarized Single-Crystal Spectroscopic Studies of the Lowest Triplet <- Singlet System in Tetrakis(1,3-diisocyanopropane)dirhodium(2+). *J. Am. Chem. Soc.* **1981**, *103*, 1593-1595.
- 44. Dallinger, R. F.; Miskowski, V. M.; Gray, H. B.; Woodruff, W. H., Metal-Metal Interactions in Binuclear Rhodium Isocyanide Complexes. Resonance Raman Spectra of the ¹A_{1g} and Eu ³A_{2u}) Electronic States of Tetrakis(1,3-diisocyanopropane)dirhodium(I). *J. Am. Chem. Soc.* **1981**, *103*, 1595-1596.
- 45. Milder, S. J.; Brunschwig, B. S., Factors Affecting Nonradiative Decay: Temperature Dependence of the Picosecond Fluorescence Lifetime of $Pt_2(pop)_4^{4-}$. *J. Phys. Chem.* **1992,** *96*, 2189-2196.
- 46. Lam, Y. C.; Gray, H. B.; Winkler, J. R., Intersystem Crossing in Diplatinum Complexes. *J. Phys. Chem. A* **2016**, *120*, 7671–7676.
- 47. Hofbeck, T.; Lam, Y. C.; Kalbáč, M.; Záliš, S.; Vlček, A.; Yersin, H., Thermally Tunable Dual Emission of the d^8 - d^8 Dimer $[Pt_2(\mu-P_2O_5(BF_2)_2)_4]^{4-}$. *Inorg. Chem.* **2016**, *55*, 2441–2449.
- 48. Chergui, M., On the interplay between the charge, the spin and the structural dynamics in transition metal complexes. *Dalton Trans.* **2012**, *41*, 13022-13029
- 49. Chergui, M., Ultrafast Photophysics of Transition Metal Complexes. *Acc. Chem. Res.* **2015**, *48*, 801–808.
- 50. Bräm, O.; Messina, F.; El-Zohry, A. M.; Cannizzo, A.; Chergui, M., Polychromatic femtosecond fluorescence studies of metal—polypyridine complexes in solution. *Chem. Phys.* **2012**, *393*, 51–57.
- 51. Cannizzo, A.; van Mourik, F.; Gawelda, W.; Zgrablic, G.; Bressler, C.; Chergui, M., Broadband Femtosecond Fluorescence Spectroscopy of [Ru(bpy)₃]²⁺. *Angew. Chem. Int. Ed.* **2006**, *45*, 3174-3176.
- 52. Bräm, O.; Messina, F.; Baranoff, E.; Cannizzo, A.; Nazeeruddin, M. K.; Chergui, M., Ultrafast Relaxation Dynamics of Osmium–Polypyridine Complexes in Solution. *J. Phys. Chem. C* **2013**, *117*, 15958–15966.
- 53. Auböck, G.; Chergui, M., Sub-50-fs photoinduced spin crossover in $[Fe(bpy)_3]^{2+}$. *Nat. Chem.* **2015**, *7*, 629-633.
- 54. Cannizzo, A.; Blanco-Rodríguez, A. M.; Nahhas, A.; Šebera, J.; Záliš, S.; Vlček, A., Jr.; Chergui, M., Femtosecond Fluorescence and Intersystem Crossing in Rhenium(I) Carbonyl-Bipyridine Complexes *J. Am. Chem. Soc.* **2008**, *130*, 8967-8974.
- 55. El Nahhas, A.; Cannizzo, A.; van Mourik, F.; Blanco-Rodríguez, A. M.; Záliš, S.; Vlček, A., Jr.; Chergui, M., Ultrafast Excited-State Dynamics of [Re(L)(CO)₃(bpy)]ⁿ Complexes: Involvement of the Solvent *J. Phys. Chem. A* **2010**, *114*, 6361-6369.
- 56. El Nahhas, A.; Consani, C.; Blanco-Rodríguez, A. M.; Lancaster, K. M.; Braem, O.; Cannizzo, A.; Towrie, M.; Clark, I. P.; Záliš, S.; Chergui, M.; Vlček, A., Jr., Ultrafast Excited-State Dynamics of Rhenium(I) Photosensitizers [Re(Cl)(CO)₃(N,N)] and [Re(imidazole)(CO)₃(N,N)]⁺: Diimine Effects. *Inorg. Chem.* **2011**, *50*, 2932–2943.
- 57. Mai, S.; González, L., Unconventional Two-Step Spin Relaxation Dynamics of [Re(CO)₃(im)(phen)]⁺ in Aqueous Solution. *Chem. Sci.* **2019**, *10*, 10405–10411.

58. Mewes, L.; Ingle, R. A.; Megow, S.; Böhnke, H.; Baranoff, E.; Temps, F.; Chergui, M., Ultrafast Intersystem Crossing and Structural Dynamics of $[Pt(ppy)(\mu^{-t}Bu_2pz)]_2$. *Inorg. Chem.* **2020**, *59*, 14643–14653.

TOC graphic



Synopsis

Singlet $d\sigma^*p\sigma$ and higher electronic excited states of d^8d^8 di-isocyanides decay through excitation-wavelength-specific relaxation cascades to the lowest $d\sigma^*p\sigma$ triplet state. The lowest singlet $d\sigma^*p\sigma$ excited state is largely bypassed during decay of states populated upon UV excitation. Direct decay from these higher lying states to the ground state also is observed. Owing to electron-density delocalization, ligand $C\equiv N$ vibrations are sensitive reporters of excited-state decay processes.